Zahn, R., Comas, M.C., and Klaus, A. (Eds.), 1999
Proceedings of the Ocean Drilling Program, Scientific Results, Vol. 161

19. PRESSURE-TEMPERATURE EVOLUTION OF THE METAMORPHIC BASEMENT OF THE ALBORAN SEA: THERMOBAROMETRIC AND STRUCTURAL OBSERVATIONS[1]

Juan I. Soto,[2] John P. Platt,[3] M. Sánchez-Gómez,[2] and José M. Azañón[2]

ABSTRACT

The continental basement of the Alboran Sea basin, drilled by Ocean Drilling Program Leg 161 at Site 976 (Holes 976B and 976E), consists of a high-grade metapelitic sequence with thin interlayers of marble and a few leucogranite dikes. A major tectonic boundary with fault gouges and cataclastic rocks divides the basement section into two parts: an upper section (~125 m thick) that was mainly formed by high-grade schists, and a lower section (with a minimum thickness of 135 m) that contains abundant gneissic rocks. The high-grade schist sequence comprises interlayered metapelites with different bulk compositions, including Al-rich metapelites (corundum-bearing schists: biotite + corundum + sillimanite + andalusite + K-feldspar + plagioclase + ilmenite ± garnet) and Fe-rich metapelites with or without staurolite (staurolite-bearing schist: staurolite + biotite + garnet + sillimanite + andalusite + K-feldspar + plagioclase + ilmenite + quartz; biotite-rich schist: biotite + garnet + sillimanite + andalusite + plagioclase + ilmenite + quartz). The gneissic sequence (biotite + cordierite ± garnet + sillimanite + andalusite + K-feldspar + plagioclase + ilmenite + magnetite + quartz) has abundant migmatite textures (stromatic and agmatitic textures). The high-grade schist has a strong foliation (S_2) defined by sillimanite + biotite + plagioclase, which could be correlated with the gneissic foliation in the gneiss, although the latter was subsequently modified by compaction and further deformation during partial melting. Textural relationships define three major assemblages in the high-grade schist: assemblage 1 (post-D_1), with garnet I + staurolite + biotite + plagioclase + quartz; assemblage 2 (D_2), with biotite + sillimanite + K-feldspar + plagioclase + quartz; and assemblage 3 (post-D_2), with biotite + andalusite + K-feldspar + plagioclase + quartz. A large growth of garnet (garnet II) also occurs after D_2. The present assemblage in the gneiss with sillimanite + andalusite + cordierite ± garnet + biotite + muscovite + K-feldspar + plagioclase + quartz, probably results from a series of strongly overstepped reactions that occurred during melting. Standard geothermometers (in particular, garnet-biotite) used in these rocks give spurious results. The textural evidence as well as the variability of the thermobarometric results indicate that many of the observed mineral assemblages are not in equilibrium. We suggest two distinctive pressure-temperature (PT) paths constrained by phase relations, one for the high-grade schist and one for the gneiss. The PT conditions during D_2 in the high-grade schist achieved high temperature under low-pressure conditions (3 kbar at 650°–700°C), with a minimum pressure drop of 4 kbar. In the gneiss, melting occurred at 5–3 kbar and 700°–750°C. The decompression PT path was followed by near-isobaric cooling (P < 3 kbar), which produced quick crystallization of residual melts in the andalusite stability field (T ~ 600°C).

INTRODUCTION

The Alboran Sea in the western Mediterranean is one of several extensional basins of late Tertiary age that formed in close association with the compressional orogens of the Alpine system. These include the Aegean Sea, the Pannonian Basin, the Tyrrhenian Sea, and the Balearic Basin. Like these basins, the Alboran Sea basin is partly surrounded by an arcuate mountain chain formed by the Betic Cordillera (southern Spain) and the Maghrebian Chain (Rif and Tell, in Morocco; Fig. 1). Contractional deformation continued within these mountain chains during basin formation. The Alboran Sea basin appears to have formed on the extended and thinned remains of a late Mesozoic to Paleogene orogen (known as the Alboran Domain) that forms the Internal Zones of the surrounding Betic Cordillera and Rif mountain chains (Fig. 1). Contraction continued in the External Betic and Rif belts during the Neogene evolution of the basin to form the present arcuate structure (e.g., Platt and Vissers, 1989; Comas et al., 1992; García-Dueñas et al., 1992; Watts et al., 1993).

One of the objectives of Ocean Drilling Program (ODP) Leg 161 was to investigate the basement of the Alboran Sea basin, as its nature, structural history, and thermal evolution provide important constraints for constructing rifting models for the region and for testing the various tectonic hypotheses (Comas, Zahn, Klaus, et al., 1996; Platt et al., 1996). To allow substantial penetration of the acoustic basement, Site 976 was located on a basement high (Fig. 1), covered by a thin, discontinuous, sedimentary sequence (2- to 2.4-s two-way travel time) of middle Miocene to Pliocene–Pleistocene age (Shipboard Scientific Party, 1996). This basement high is ~50 km long and 15 km wide, and was partially drilled during Leg 13 at Deep Sea Drilling Project Site 121 (Ryan, Hsü, et al., 1973). The orientation of this basement high changes southward from northeast–southwest, at Site 976, to north-northwest–south-southeast. Interpretation of multichannel commercial seismic profiles indicates that this basement elevation corresponds to a horst limited by north–south- and northeast–southwest-trending normal faults, bounding a major depocenter with up to 8 km of lower Miocene–Pleistocene sediments toward the west (Comas et al., 1992; Watts et al., 1993; de la Linde et al., 1996; Soto et al., 1996).

During Leg 161, the *JOIDES Resolution* crew drilled into the acoustic basement at Site 976 (Holes 976B and 976E), where we succeeded in penetrating and sampling 258.97 m (in Hole 976B, 1108.0 m water depth, from 669.73 to 928.70 m below seafloor [mbsf]) and 84.22 m (in Hole 976E, 1107.6 m water depth, from 652.08 to 736.30 mbsf) of high-grade metamorphic rocks, including high-grade pelitic schist, pelitic gneiss, migmatite, and granite dikes, together with minor amounts of marble and calc-silicate rocks (Shipboard Scientific Party, 1996; Fig. 2). A thin (up to 15 cm thick) marine clastic sequence of middle Miocene age (Serravallian; Zone NN7) lies directly on top of the basement rocks in Holes 976B (669.73 mbsf) and 976E

[1]Zahn, R., Comas, M.C., and Klaus, A. (Eds.), 1999. *Proc. ODP, Sci. Results*, 161: College Station, TX (Ocean Drilling Program).
[2]Instituto Andaluz de Ciencias de la Tierra and Departamento de Geodinámica, C.S.I.C.-Universidad de Granada, 1807-1-Granada, Spain. jsoto@goliat.ugr.es
[3]Department of Geological Sciences, University College London, Gower Street, London WC1E 6BT, United Kingdom.

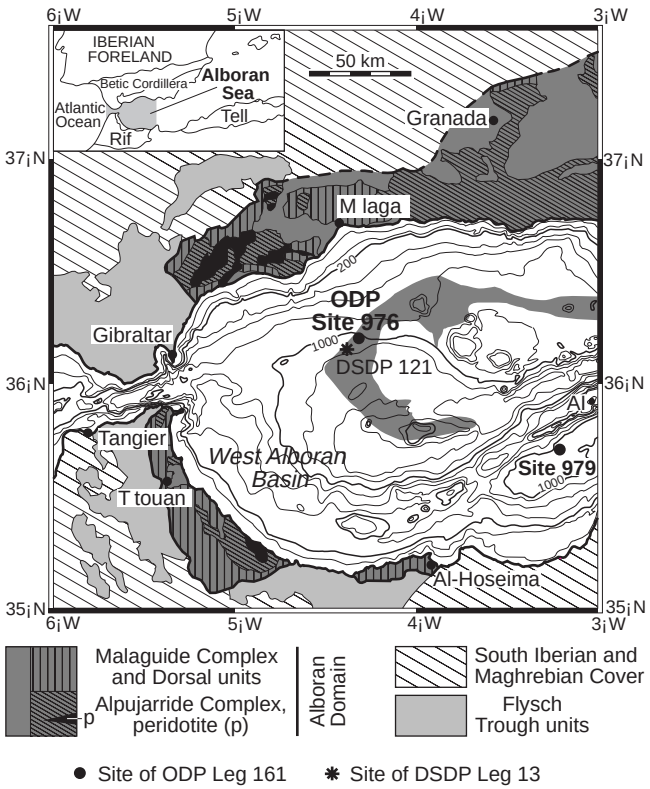

Figure 1. Location of Sites 976 and 121 in the West Alboran Sea basin, with a schematic geologic map of the surrounding Betic Cordillera and Rif mountain chains. The metamorphic basement high around Site 976 is shown in shading (from Comas et al., 1993), similar to the outcropping Alpujárride Complex of the Alboran Domain, closely associated with bodies of exhumed mantle peridotite (shown in black). Bathymetric contour interval is 200 m. AI = Alboran Island.

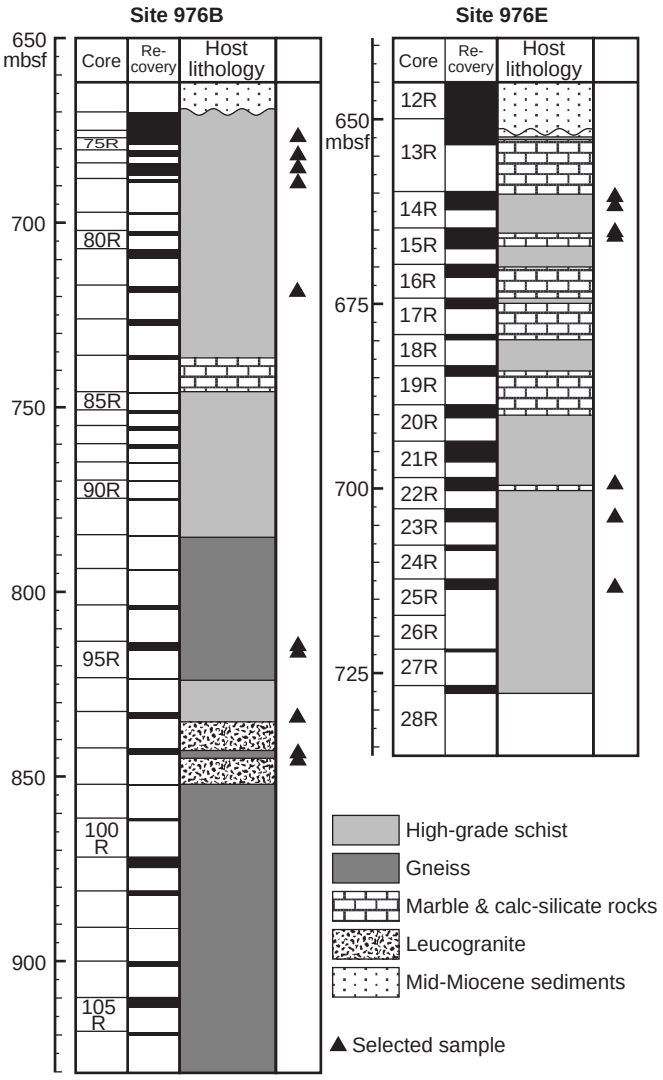

Figure 2. Lithologic columns of the basement cored in Holes 976B and 976E (modified from Shipboard Scientific Party, 1996). The locations of samples analyzed by microprobe are shown for reference.

(652.08 mbsf). This contact appears to be an unconformity. Nevertheless, the presence of breccias with a calcareous or dolomitic matrix with microfossils down to 40 m below the contact (705 mbsf at Hole 976B and 695 mbsf at Hole 976E) and a significant difference in depth for this contact between Holes 976B and 976E are indicative of active faulting of the basement-sediment contact during middle Miocene sedimentation (Shipboard Scientific Party, 1996; Comas and Soto, Chap. 25, this volume).

This paper reports the results of post-cruise petrologic and microstructural studies on basement samples recovered from Site 976 (Holes 976B and 976E). The characterization of the principal stages of the metamorphic evolution (in terms of changes in intensive variables such as P and T) in the basement is based on detailed study of a selected number of samples. Textural observations and petrologic studies based on the characterization of the mineral chemistry by microprobe analyses have been performed. The determination of the metamorphic pressure-temperature conditions in marble and calc-silicate intercalations are presented in an accompanying paper by López Sánchez-Vizcaíno and Soto (Chap. 18, this volume).

SUMMARY OF BASEMENT ROCKS AT SITE 976

The top 115 m of basement cored at Hole 976B (down to 785 mbsf; Fig. 2) consists of dark gray, quartz-biotite-sillimanite-plagioclase pelite schist, with visible porphyroblasts of garnet and andalusite (referred to as high-grade schist). This metapelite sequence has interlayers of calcite and dolomite marble and associated calc-silicate rocks (particularly abundant in Cores 161-976B-81R and 83R–85R) as reaction bands that developed between the metapelite-metacarbonate contacts (see López Sánchez-Vizcaíno and Soto, Chap. 18, this volume). This sequence passes downward into a banded pelitic gneiss, locally migmatitic, with irregular veins and segregations of granitic material (e.g., Sections 161-976B-95R-2, 95R-3; Cores 161-976B-98R; 101R, and 102R). The term gneiss is used to designate medium gray, more massive rocks with large porphyroblasts of K-feldspar, plagioclase, cordierite, quartz, and andalusite. Both rock units are cut by peraluminous, leucogranitic dikes (e.g., Cores 161-976B-81R and 82R in the high-grade schist and Cores 161-976B-93R and 97R–107R in the gneiss). The high-grade schist and the gneiss at Hole 976B are probably separated by a significant tectonic boundary, represented by a thick band (up to 20 m thick) of fault rocks (consolidated clay breccia, fault gouges, and cataclastic rocks; from Cores 161-976B-86R–88R, 91R, and 92R) (see Comas and Soto, Chap. 25, this volume).

The basement sequence at Hole 976E consists of an upper section of 30 m of interlayered high-grade, biotite-rich schist, marble, and

calc-silicate rocks (down to 692.9 mbsf; see Fig. 2). The hole grades into more homogeneous high-grade schist with a few thin intercalations (10–20 cm thick) of marble and calc-silicate rocks (Section 161-976E-21R-3). Gneiss and migmatite gneiss were not found in this hole, probably because of shallower penetration compared with Hole 976B. The only granite bodies encountered in Hole 976E are found as small fragments in Sections 161-976E-13R-2, 22R-3, 23R-1, and 24R-1.

The lithologic association and metamorphic characteristics at the site broadly resemble those in parts of the Alpujárride Complex in the adjacent Betic Cordillera (and its counterparts in the Rif, the Sebtides). A sequence formed by biotite + K-feldspar + sillimanite-rich pelitic schist, granular cordierite-bearing gneiss, and marble intercalations, which is commonly cut by leucogranite dikes, characterizes those units underlying the Ronda peridotite slab, some 80 km north of Site 976 (Fig. 1). These units reach upper amphibolite-to-granulite facies conditions, with evidence of melting under high-temperature and relatively low-pressure metamorphic conditions (Mollat, 1968; Buntfuss, 1970; Loomis, 1972; Westerhof, 1977; Lundeen, 1978; Sánchez-Gómez et al., 1995; Sánchez-Gómez et al., Chap. 23, this volume).

MINERAL ASSEMBLAGES AND DUCTILE FABRICS

Most of the high-grade schist is very biotite- and sillimanite-rich and garnet- and staurolite-poor. Graphite is a major component and is also included in mica and Al-silicate porphyroblasts. The lithologic sequence consists of garnet- and staurolite-rich layers (staurolite-bearing schist) with an Fe-rich bulk composition; layers with biotite and fibrolite (sillimanite crystals ≤10 µm in minimum dimensions, following Kerrick and Speer, 1988) without plagioclase (biotite-rich schist); and corundum-bearing and quartz-and-staurolite-lacking layers, with a more aluminous and silica-poor bulk composition (corundum-bearing schist). Corundum-bearing schist is usually found near calc-silicate reaction bands (e.g., Sample 161-976B-76R-1, Piece 9A, 77–80 cm; Sample 161-976B-77R-2, Piece 3A, 20–25 cm; Sample 161-976B-76R-1, Piece 9A, 77–80 cm). Quartz, plagioclase, biotite, and Al-silicates (andalusite and sillimanite) are always present as major components of the high-grade schist. Apatite, ilmenite, zircon, pyrite, and pyrrhotite (in late veins and as a transformation product of pyrite) are minor and accessory minerals. Tourmaline is a major component in some of the corundum-bearing high-grade schist. Chlorite, muscovite, and hematite are retrograde minerals. Kyanite has not been observed in any of the high-grade schist samples.

The pelitic gneiss consists of medium gray biotite-bearing gneiss, with K-feldspar, sillimanite, andalusite, and cordierite porphyroblasts. Tourmaline, apatite, zircon, magnetite, Ti-magnetite, and ilmenite are accessory components. Muscovite is locally present, particularly in veins, migmatitic segregations, and tension fractures in large andalusite porphyroblasts (up to 2–3 cm long). Small idiomorphic garnet porphyroblasts (up to 500 µm) have been found in some samples, associated with large concentrations of magnetite and Ti-magnetite (e.g., Samples 161-976B-98R-1, 38–40 cm, and 98R-1, 96–101 cm). Millimeter-long lenses of felsic material, as well as broader scale compositional layering, mineral orientation, and abundant quartz-tourmaline and felsic veins, define the main metamorphic foliation. Much of the gneiss is migmatitic, with cm-thick veins and segregations of weakly foliated or unfoliated felsic material (leucosome) containing large crystals of cordierite, as well as biotite, andalusite, fibrolite, magnetite, and tourmaline. The leucosome domains are composed of K-feldspar, plagioclase, and quartz in granitic proportions. Zoned tourmaline porphyroblasts are always present as a minor component. These mostly occur as stromatic migmatites (terminology of Mehnert, 1968; and McLellan, 1983), which implies that melting was controlled by a strong, compositional foliation before melting. In some instances, leucosome also occurs as veins crosscutting the foliation and in pull-aparts. This locally gives the gneiss a brecciated appearance (agmatitic textures; e.g., Sample 161-976B-95R-3, Piece 7, 53–63 cm).

Following are the most complete assemblages in the high-grade schist and gneiss (mineral abbreviations after Kretz, 1983):

1. biotite-rich schist: biotite (Bt) ± garnet (Grt) + fibrolite (Fib) ± andalusite (And) + K-feldspar (Kfs) + plagioclase (Pl) + ilmenite (Ilm) + quartz (Qtz);
2. staurolite-bearing schist: staurolite (St) + Bt + Grt + Fib + And + Kfs + Pl + Ilm + spinel (Spl) ± rutile (Rt) + Qtz;
3. corundum-bearing schist: Bt ± Grt + Fib + And + corundum (Crn) + Kfs + Pl + Ilm; and
4. banded pelitic gneiss: Bt ± Grt + cordierite (Crd) + Fib + And + Kfs + Pl + Ilm + magnetite (Mag) + Qtz.

There are reaction textures among the AFM (Al_2O_3-FeO-MgO) mineral phases, and in particular the Al-silicates, present in all the high-grade schists. Thus, these mineral assemblages are not in equilibrium assemblages. Nevertheless, the high-grade schist assemblage with St + Bt + Grt + And + Sil ± Kfs clearly reflects lower temperatures than the Bt + Crd + And + Sil + Kfs assemblage in the gneiss.

Ductile Fabrics

Two sets of ductile fabrics and structures can be distinguished in the high-grade schist, referred to as D_1 and D_2. The earlier fabric, S_1, is characterized by compositional layering, transposed quartz veins, 0.5- to 2-mm-scale quartz-rich and biotite-rich laminae and oriented biotite. Garnet, staurolite, and early plagioclase porphyroblasts have grown over S_1 and include it as graphite trails.

S_1 has been intensively affected by 1- to 50-mm-scale D_2 folds. These are commonly tight and asymmetric, but may also be symmetric. The compositional layering and quartz-biotite laminae that define S_1 are considerably thickened in the hinges of the folds relative to the limbs. Biotite is recrystallized in the fold hinges, and tends to lie parallel to the axial surface, as do elongate mats of fibrolite; together, the two define a weak axial planar fabric, S_2 (Pl. 1, figs. 1, 2). In much of the high-grade schist, D_2 has transposed completely the S_1 fabric. D_2 was followed by static crystallization of andalusite, plagioclase, a second garnet, and K-feldspar.

We have observed no clear transition between the fabrics in the high-grade schist and that in the gneiss, as there is significant faulting along the boundary between these two lithotypes (Comas and Soto, Chap. 25, this volume). Thus, relative age relationships of the gneissic foliation in relation to the deformational history of the schist is uncertain. On the basis of the textural relationships discussed below, we believe that it is a composite foliation, which may have formed initially at about the same time as D_2 in the high-grade schist, but was subsequently modified by compaction or further deformation during partial melting.

TEXTURAL RELATIONSHIPS

The textural observations for the two rock types encountered are described for every individual phase in relation to the different ductile fabrics.

High-Grade Schist

Al_2SiO_5 Polymorphs

Sillimanite occurs as elongated fibrolitic mats, and in places as larger prismatic porphyroblasts. Both textural types of sillimanite define the S_2 planar fabric. Fibrolite forms in the matrix aggregates with

submicroscopic intergrowths of K-feldspar and plagioclase. In many cases, these fibrolite aggregates are intergrown with biotite (Pl. 1, fig. 5). In these aggregates, needle-shaped crystals of fibrolite are parallel to the external foliation (harmonious fibrolite-type; Vernon and Flood, 1977), although there are abundant small fibrolite crystals in the matrix, which are largely oblique to the S_2 foliation (disharmonious fibrolite-type; Pl. 1, fig. 5). Andalusite forms large randomly oriented porphyroblasts (up to 2–3 cm long) that grew postkinematically with respect to S_2. It commonly contains oriented inclusions of ilmenite, biotite, and fibrolite parallel to S_2 (Pl. 2, fig. 6), and corroded staurolite porphyroblasts partially transformed to ilmenite and minor spinel (Pl. 2, fig. 5). Andalusite commonly shows irregular outlines interfingering with plagioclase and K-feldspar, and locally occurs as rounded blebs included in these minerals. Andalusite is also locally altered to randomly oriented white mica.

Garnet

We have clearly identified (see also Shipboard Scientific Party, 1996) two families of garnet porphyroblasts on the basis of textural relationships with S_2. Garnet I usually has graphitic and opaque mineral (ilmenite) inclusion trails defining an internal foliation (S_1) oblique to the external S_2 foliation. This internal foliation is straight in the central part of the crystals, suggesting interkinematic garnet growth between D_1 and D_2 (Pl. 2, figs. 1, 3). Garnet I porphyroblasts can be partially corroded to andalusite, plagioclase, and biotite, and in some cases to a fine-grained aggregate of chlorite-muscovite-Na-rich plagioclase-quartz (e.g., Sample 161-976E-14R–1, 98–102 cm; Pl. 2, fig. 4). Many garnet I porphyroblasts have an inclusion-poor outer zone with idiomorphic outlines (garnet II). This outermost rim usually has fibrolite inclusions that are continuous with the matrix (Pl. 2, fig. 3). In some grains, the boundary between the two zones is irregular and shows evidence of resorption (e.g., Sample 161-976E-15R-1, 02–07 cm; Pl. 2, fig. 2). Garnet II grains without garnet I cores also occur in the matrix as large (up to 1 cm long), idiomorphic porphyroblasts with abundant inclusions parallel to the external S_2 foliation. Garnet II includes fibrolite, biotite, plagioclase, K-feldspar, tourmaline (Pl. 2, fig. 3), and in places staurolite and corundum (e.g., Sample 161-976B-76R-1, 45–49 cm).

Plagioclase

Plagioclase occurs as inclusions in garnet I and garnet II porphyroblasts, and as large porphyroblasts in the matrix (up to 5–7 mm long). In the matrix, plagioclase has two main growth stages. The first, plagioclase I, is represented by cores crowded with linear inclusion trails of graphite, opaque minerals, biotite, and tourmaline (Pl. 1, figs. 3, 4). The straight internal foliation indicates interkinematic growth between D_1 and D_2, although locally plagioclase I grows over D_2 microfolds (early syn-D_2 growth). Plagioclase II occurs as inclusion-free rims of porphyroblasts with local inclusions of K-feldspar and biotite. It rarely contains inclusions of fibrolite, parallel to S_2, indicating growth at a late stage (post-D_2). Plagioclase together with K-feldspar occurs also in the matrix including resorbed blebs of andalusite.

K-Feldspar

K-feldspar occurs in different textures: finely intergrown within fibrolite mats, interstitially with quartz in late veins cutting across the S_2 foliation, as large irregular poikiloblasts, and as thin rims surrounding zoned plagioclase porphyroblasts. K-feldspar occurs in some places as intergrowths with plagioclase within garnet II porphyroblasts.

Biotite

Dark brown biotite porphyroblasts occur in very different textures: oriented parallel to S_1 and to S_2 in the hinge areas of D_2 folds (Pl. 1, figs. 1, 2), as straight inclusion trails in plagioclase II and garnet II porphyroblasts (Pl. 2, fig. 3), and as reaction products of garnet I and staurolite (Pl. 2, fig. 4). Biotite porphyroblasts defining the S_2 are closely related to fibrolite and commonly occur as intergrowths (Pl. 1, fig. 5). Mimetic growth of chlorite at the expense of biotite has also been observed (e.g., Sample 161-976B-76R-1, 03–07 cm). Large porphyroblasts of biotite with pyrite inclusions partially transformed to pyrrhotite are common in the corundum-bearing schist (e.g., Sample 161-976B-77R-2, 24–26 cm). All of these textural relationships indicate that biotite was stable during the entire metamorphic evolution of these rocks, and biotite with K-feldspar from late D_2 onward.

Staurolite

Staurolite is present in two different textures that are both observed in the same rock sample (e.g., Sample 161-976B-76R-1, 45–49 cm). Small staurolite crystals (<200 µm) are preserved as corroded inclusions in garnet II and andalusite porphyroblasts. In andalusite, staurolite is in places transformed into an Fe-rich spinel (hercynite; Pl. 2, fig. 5). In some cases, it is observed as nontransformed crystals in the matrix with an internal foliation characterized by straight inclusions of graphite and ilmenite (Pl. 1, fig. 6). Both textural positions suggest that staurolite grew interkinematically between D_1 and D_2 and was involved in some of the garnet-producing reactions.

Corundum

Corundum is present as elliptical porphyroblasts (up to several mm long) in quartz-poor assemblages. Corundum crystals have inclusion trails of graphite and ilmenite that are generally continuous with S_2 (e.g., Sample 161-976B-77R-2, 24–26 cm).

Ti-Fe Oxides

Ilmenite is a major constituent in all the different types of high-grade schist. It is present in the matrix, parallel to S_2, or as inclusions in garnets I and II, plagioclase, andalusite, corundum, staurolite, and K-feldspar porphyroblasts. Wormlike crystals of ilmenite in a radial pattern are common inside andalusite. Rutile is only present as needle-shaped crystals preserved in large ilmenite grains, suggesting that rutile was transformed into ilmenite before D_2. Another minor Fe-rich oxide present is hercynite, which commonly occurs as small grains in poikiloblastic andalusite and plagioclase.

Pelitic and Migmatite Gneiss

Al_2SiO_5 Polymorphs

Fibrolite and coarse, prismatic sillimanite are common fabric-forming elements in the gneiss. They form dense, monomineral aggregates, which are particularly well developed on the margins of leucosome segregations (harmonious fibrolite-type; Vernon and Flood, 1977; Pl. 3, fig. 1). In leucosome veins, minor fibrolite needles are also present without preferential orientation, growing over K-feldspar and plagioclase (disharmonious fibrolite-type; Pl. 3, fig. 5; Pl. 4, fig. 3). Andalusite shows contradictory textural relationships with the main foliation in the gneiss. Andalusite porphyroblasts contain oriented inclusion trails of ilmenite, usually oblique to the external foliation, or in some cases, they include oriented fibrolite crystals parallel to the external foliation (see also Shipboard Scientific Party, 1996). This can be interpreted as growth of andalusite after silliman-

ite, but that deformation continued also after andalusite growth. Other textural evidence in leucosome veins supports the view that andalusite coexisted with a melt phase. This evidence includes andalusite present as small and partially resorbed fragments of single crystals, surrounded by a granitic matrix formed by K-feldspar, quartz, and plagioclase (Pl. 4, fig. 3); in places andalusite is partially replaced by cordierite (Pl. 4, fig. 6); and subhedral andalusite, together with quartz, is sometimes included in large porphyroblasts of K-feldspar (Pl. 4, fig. 4). These textures could be interpreted as magmatic andalusite in a low-T crystallizing granitic melt (e.g., Vernon, 1986).

Garnet

Garnet is a minor component of the migmatite gneiss, occurring in two textures: either as corroded relics largely transformed to plagioclase, K-feldspar, pyrite, magnetite, and quartz (garnet I; Pl. 3, fig. 3), or as small euhedral porphyroblasts partially surrounded by magnetite (garnet II; Pl. 3, fig. 4). Some of the gneissic rocks with cordierite contain corroded garnet porphyroblasts. The disappearance of garnet in those samples with cordierite suggests that garnet is consumed in the cordierite-forming reactions.

Plagioclase and K-Feldspar

Both feldspars occur as idiomorphic grains in the matrix of leucosome domains. Plagioclase porphyroblasts with zoning patterns similar to those described in the high-grade schist are preserved in the pelitic domains. The two textural positions of plagioclase could be interpreted as relic "metamorphic" crystals in pelitic (restitic) domains, and new "granitic" plagioclase coexisting with K-feldspar in leucosome domains. K-feldspar also occurs as subhedral phenocrysts with inclusion-rich cores (Pl. 4, fig. 4).

Biotite

This mineral occurs in two textures, with both optical and mineral assemblage differences. In pelitic domains of the gneiss, biotite occurs as dark brown porphyroblasts, oriented parallel to the foliation, and closely related to oriented fibrolite mats. In leucosome domains, in contrast, biotite occurs as light green porphyroblasts forming decussate clusters with large magnetite and Ti-magnetite cubic grains. These biotite crystals usually have cleavage-parallel oriented inclusions of spinel transformed to ilmenite and rutile (Pl. 4, fig. 2).

Cordierite

Cordierite is present in the leucosome domains as large, irregular porphyroblasts of up to 1–2 cm long (Pl. 4, fig. 1). It mostly appears to postdate the main foliation (Pl. 3, fig. 6). Cordierite includes surrounding porphyroblasts from the K-feldspar, plagioclase, biotite, quartz (Pl. 4, fig. 5), and corroded andalusite matrix (Pl. 4, fig. 6). It is commonly corroded and altered to pinnite and also to coarse-grained muscovite. Cordierite is more abundant in those domains with scarce to absent biotite, indicating that biotite, together with garnet (see above comment), is partially involved in the cordierite-forming reactions.

Ti-Fe Oxides

Idiomorphic cubes of magnetite and Ti-magnetite are the most abundant oxides in the pelitic and migmatite gneiss. They usually occur as large porphyroblasts included in fibrolite and biotite aggregates (Pl. 3, fig. 2), andalusite, and relic garnet I. Ilmenite is a minor component of the gneiss, and it appears included in garnet I and biotite porphyroblasts. Some of these ilmenite crystals probably have submicroscopic intergrowths with rutile.

MINERAL CHEMISTRY

To characterize the mineral chemistry associated with different textures described, we selected 15 samples for microprobe analyses (see Fig. 2 for their location in the basement section). The samples were analyzed in the electron microprobe Cameca SX50 at the University of Granada. An acceleration voltage of 15 kV, beam current of 20 nA, and beam diameter of 8 µm were used. Standards were simple synthetic oxides (Al_2O_3, Fe_2O_3, Cr_2O_3, $MnTiO_4$, and MgO) and natural silicates (albite, orthoclase, wollastonite), and sphalerite. Data were reduced using the PAP procedure ($\phi(\rho z)$ procedure) supplied by the manufacturers (Pouchou and Pichoir, 1985).

In this paper, we present the main characteristics of the mineral chemistry data for every major mineral phase, and combine the data from high-grade schist with those from pelitic and migmatite gneiss.

Garnet

Garnet porphyroblasts have a large chemical variation (Figs. 3, 4; Table 1). Metapelite garnets usually have variable Fe, Ca, and Mn contents, with a low and constant Mg content. Garnets from gneissic rocks are very close in composition to those from the high-grade schist. (Because we have normalized all the garnet analyses to a mineral chemical formula with 12 oxygens and $Fe_{total} = Fe^{2+}$ [see Table 1], all the iron contents described in this paper should be considered as the sum of almandine and andradite end-member contents.)

The two garnet types distinguished in the staurolite-bearing high-grade schist each have distinctive zoning pattern. Garnet I porphyroblasts have a normal zoning pattern indicating prograde growth: decreasing spessartine and increasing almandine content from core to rim ($Alm_{0.65–0.80}$ $Grs_{0.05–0.20}$ $Pyr_{0.02–0.06}$ $Sps_{0.05–0.13}$; Figs. 3A, 4A). Garnet II rims and grains have a fairly constant composition (Figs. 3B, 4B), similar to the rims of garnet I, but with some sharp increases in spessartine and grossular at the rims (i.e., inverse zoning patterns; up to $Alm_{0.62}$ $Grs_{0.22}$ $Pyr_{0.04}$ $Sps_{0.12}$). Incomplete or truncated zoning patterns are present in grains included in andalusite porphyroblasts (garnet II) and partially corroded garnet I grains.

Garnets from corundum-bearing schist have a higher grossular content ($Grs_{0.20–0.35}$) and a low spessartine content ($Sps_{0.12–0.15}$), with low pyrope ($Pyr_{0.05–0.08}$). These garnets have a normal zoning pattern, characterized by increasing almandine content and decreasing spessartine content from core to rim (Fig. 3C). Grossular content decreases toward the rims (Fig. 4C).

Garnet in gneiss has two distinctive textures and chemical compositions (Figs. 3E, 4E). Relict and corroded garnet I porphyroblasts have a large chemical variation ($Alm_{0.72–0.81}$ $Grs_{0.07–0.10}$ $Pyr_{0.06}$ $Sps_{0.06–0.15}$), similar to the zoning pattern of garnet I from high-grade schist. Garnet II porphyroblasts have reverse zoning patterns, characterized by high and increasing spessartine content ($Sps_{0.10–0.16}$), decreasing almandine content ($Alm_{0.82–0.76}$) toward the rims, and low and constant abundance of grossular and pyrope ($Grs_{0.03}$ $Pyr_{0.04}$).

Plagioclase and K-Feldspar

The compositional range of plagioclase in all rock types is presented in Figure 5 and Table 2. Plagioclase in high-grade schist has high to medium An contents (especially in corundum-bearing rocks; $X_{An} = 0.95–0.60$). In gneissic rocks, in contrast, plagioclase has moderate An content, within a small variational range ($X_{An} = 0.50–0.35$),

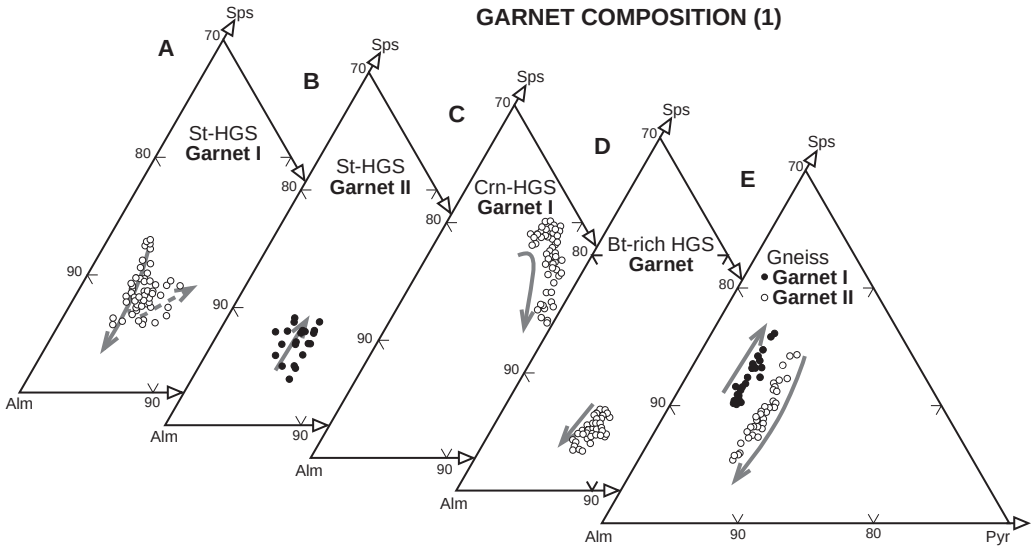

Figure 3. Garnet compositions in metapelitic rocks are plotted as a function of almandine (Alm), spessartine (Sps), and pyrope (Pyr) end-members. Projection is from grossular. Light gray arrows indicate core-to-rim variations. Arrow length is proportional to the amount of compositional variation between cores and rims. Broken arrow in (**A**) shows the rim composition of garnet I grains with an outermost rim similar in composition to garnet II. Mineral abbreviations after Kretz (1983). HGS = high-grade schist.

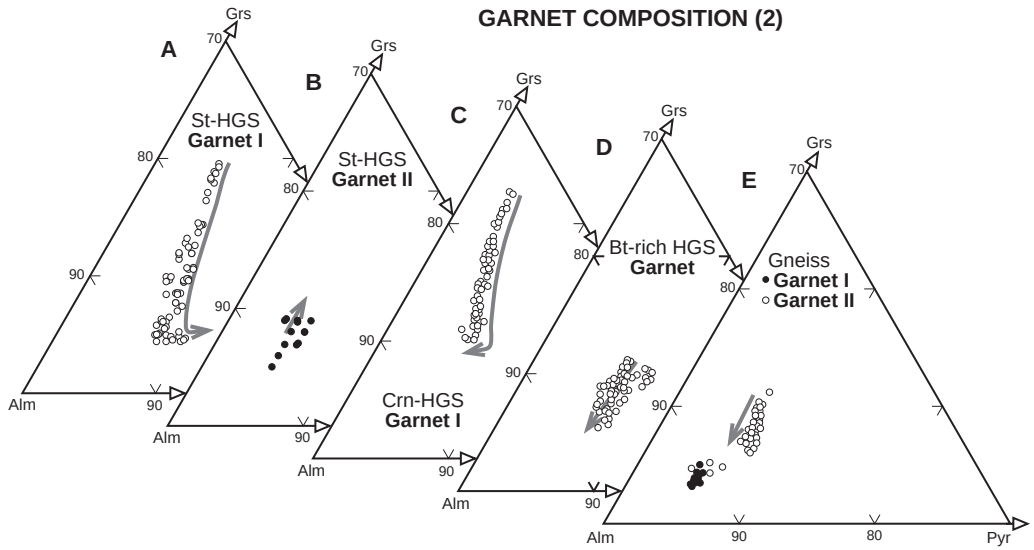

Figure 4. Garnet compositions in metapelitic rocks are plotted as a function of almandine (Alm), grossular (Grs), and pyrope (Pyr) end-members. Projection is from spessartine. Light gray arrows indicate core-to-rim variations. Arrow length is proportional to the amount of compositional variation between cores and rims. Mineral abbreviations after Kretz (1983). HGS = high-grade schist.

similar to the Ab-rich composition of plagioclase in granite rocks (X_{An} = 0.40–0.30).

Plagioclase porphyroblasts in high-grade schist have variable zoning patterns, with oscillatory and normal zoning (i.e., more albite-rich toward rims) as the most common types. Some matrix porphyroblasts have a thin outermost rim of K-feldspar (X_{Ab} = 0.05–0.15); surrounding plagioclase II rims and with inclusions of fibrolite and biotite. The composition of plagioclase inclusions spans from X_{An} = 0.4–0.6, in garnet II porphyroblasts, to X_{An} = 0.8 in the outer rim of garnet I grains (Fig. 5A).

We have observed K-feldspar (X_{Ab} = 0.02–0.08) with plagioclase (X_{An} = 0.50–0.64) intergrowths included in the rims of garnet II porphyroblasts. This texture could be interpreted as coexisting feldspars crystallizing during subsolidus cooling, rather than as exsolution textures.

Plagioclase in leucosome veins (X_{An} = 0.38–0.44) and granite rocks (X_{An} = 0.30–0.44) has flat zoning patterns, with lower An content. Some plagioclase phenocrysts have a moderate increase in albite in the outermost rim, which can be partially surrounded by K-feldspar. Plagioclase in pelitic domains of the gneiss, however, has com-

Table 1. Representative microprobe analyses and calculated formula of garnet (single spots).

Rock type:	Staurolite-bearing high-grade schist			Corundum-bearing schist		Biotite-rich schist	Gneiss
Sample:	161-976B-76R-1, 3-7 cm	976B-76R-1, 3-7 cm	976B-76R-1, 45-49 cm	976B-77R-2, 40-42 cm	976B-77R-2, 40-42 cm	976E-14R-1, 98-102 cm	976B-98R-1, 96-101 cm
Textural position:	Garnet I core	Garnet I rim	Garnet II	Core	Rim	Garnet II rim	Garnet II core
Analytic point:	E-17	E-3	B-104	F-58	F-72	A-54	104-4
SiO_2	37.17	36.95	37.70	36.91	37.01	36.81	36.00
Al_2O_3	20.98	20.80	21.23	20.78	21.04	20.96	20.54
TiO_2	0.22	0.10	0.07	0.28	0.05	0.06	0.10
MgO	0.28	0.92	1.59	1.24	2.07	1.59	1.12
FeO	28.32	35.52	34.46	25.04	28.16	35.70	36.58
MnO	5.50	2.15	3.03	5.74	5.00	1.98	4.60
CaO	8.26	4.05	3.73	10.72	6.53	3.05	1.20
Total	100.73	100.49	101.81	100.71	99.86	100.15	100.14
Cations normalized to 12 oxygens (all Fe as Fe^{2+})							
Si	2.983	2.992	2.998	2.955	2.967	2.983	2.946
Al^{iv}	0.017	0.008	0.002	0.045	0.033	0.017	0.054
Al^{vi}	1.969	1.978	1.989	1.916	1.956	1.985	1.927
Ti	0.013	0.006	0.004	0.017	0.003	0.003	0.006
ΣY	1.982	1.984	1.993	1.933	1.959	1.988	1.933
Fe^{2+}	1.903	2.408	2.292	1.616	1.894	2.422	2.516
Mg	0.034	0.111	0.189	0.148	0.247	0.191	0.136
Mn	0.374	0.147	0.204	0.389	0.340	0.136	0.319
Ca	0.710	0.351	0.317	0.920	0.561	0.265	0.105
Σ X	3.021	3.017	3.002	3.073	3.042	3.014	3.076
Alm	0.630	0.798	0.763	0.526	0.623	0.804	0.818
Grs	0.235	0.116	0.106	0.299	0.184	0.088	0.034
Pyr	0.011	0.037	0.063	0.048	0.081	0.064	0.044
Sps	0.124	0.049	0.068	0.127	0.112	0.045	0.104
Fe/(Mg + Fe)	0.983	0.956	0.924	0.916	0.885	0.927	0.949

Notes: End-member mole fractions are calculated as [Fe^{2+}/Σ X] = Alm; [Ca/Σ X] = Grs; [Mg/Σ X] = Pyr; and [Mn/Σ X] = Sps; mineral abbreviations from Kretz (1983).

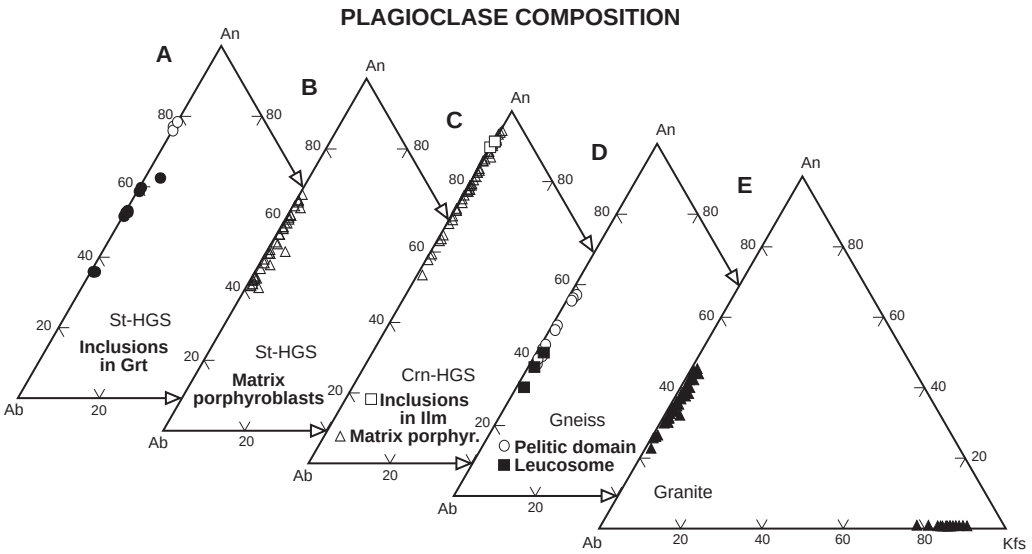

Figure 5. Plagioclase compositions in metapelitic rocks are plotted as a function of albite (Ab), anorthite (An), and K-feldspar (Kfs). Mineral abbreviations after Kretz (1983). HGS = High-grade schist.

positions close to those from high-grade schist (X_{An} = 0.50–0.58), also suggesting that it is restitic.

Biotite

Biotite has a large range in composition (see Table 3), as shown in the "ideal biotite plane" diagram of Guidotti (1984; Fig. 6). It varies between the biotite end-members annite (Al-poor, Fe-rich biotite) and siderophyllite (Al- and Fe-rich biotite). In corundum-bearing schist and gneiss, biotite tends toward the Al-rich phlogopite composition (eastonite). It is important to note that these have high-Al content ($Al^{[vi]}$ ~ 1.0 ions per formula unit [pfu]), with up to 1.3 ions pfu. These values are outside the compositional range found in natural metamorphic biotites (see Guidotti, 1984) and could be interpreted as the result of disequilibrium relationships in these rocks.

In gneiss, biotite has two distinctive compositions (Fig. 6). First, biotite from pelitic domains has a composition toward Al-rich annite [mg# ~ 0.25; mg# = Mg/(Mg + Fe)]. In contrast, biotite in leucosome

Table 2. Representative microprobe analyses and calculated formula of plagioclase (single spots).

Rock type:	Staurolite-bearing high-grade schist				Corundum-bearing schist		Gneiss		Granite	
Sample:	161-976B-74X-1, 30-34 cm	74X-1, 30-34 cm	76R-1, 45-49 cm	74X-1, 30-34 cm	77R-2, 24-26 cm	77R-2, 24-26 cm	98R-1, 96-101 cm	98R-1, 96-101 cm	82R-1, 93-98 cm	82R-1, 93-98 cm
Textural position:	Plagioclase I core	Plagioclase I rim	Included garnet II	Included garnet I	Plagioclase I core	Plagioclase I rim	Core	Rim	Core	Rim
Analytic point:	C-50	C-52	B-124	C-35	F-12	F-21	80	81	43	37
SiO_2	50.35	53.17	55.51	49.07	45.66	50.19	57.16	57.01	58.96	60.41
Al_2O_3	31.19	29.71	28.72	32.58	34.43	31.59	25.83	26.11	24.88	24.78
TiO_2	0.01	0.00	0.01	0.01	0.00	0.00	0.00	0.02	0.00	0.01
Fe_2O_3	0.12	0.18	0.30	0.31	0.04	0.23	0.00	0.17	0.00	0.04
MnO	0.00	0.03	0.05	0.07	0.01	0.01	0.01	0.01	0.00	0.00
MgO	0.01	0.00	0.00	0.00	0.00	0.00	0.00	0.00	0.00	0.00
CaO	14.35	12.66	10.77	15.82	17.96	14.66	8.49	8.67	7.29	6.91
N_2O	3.05	4.32	5.38	2.62	1.03	3.11	6.80	6.65	7.30	7.68
K_2O	0.20	0.10	0.17	0.06	0.21	0.14	0.22	0.17	0.32	0.24
Total	99.28	100.18	100.89	100.55	99.35	99.94	98.51	98.82	98.75	100.08
Cations normalized to 32 oxygens (all Fe as Fe^{3+})										
Si	9.234	9.616	9.919	8.936	8.463	9.161	10.402	10.349	10.658	10.757
Al	6.743	6.334	6.051	6.995	7.522	6.796	5.542	5.588	5.303	5.203
Ti	0.001	0.000	0.001	0.001	0.000	0.000	0.000	0.003	0.000	0.001
Fe^{3+}	0.015	0.022	0.036	0.039	0.006	0.029	0.000	0.021	0.000	0.005
Mn	0.000	0.005	0.007	0.011	0.002	0.002	0.002	0.002	0.001	0.000
Mg	0.004	0.000	0.000	0.000	0.000	0.000	0.000	0.001	0.000	0.000
Ca	2.819	2.454	2.062	3.087	3.568	2.867	1.655	1.687	1.411	1.319
Na	1.086	1.516	1.865	0.926	0.372	1.101	2.399	2.340	2.557	2.651
K	0.046	0.023	0.038	0.014	0.049	0.034	0.050	0.039	0.073	0.055
Σ Z	19.949	19.970	19.980	20.009	19.982	19.989	20.049	20.029	20.003	19.991
Ab	0.275	0.380	0.470	0.230	0.093	0.275	0.585	0.576	0.633	0.659
An	0.714	0.615	0.520	0.767	0.895	0.717	0.403	0.415	0.349	0.328
Or	0.012	0.006	0.010	0.003	0.012	0.008	0.012	0.010	0.018	0.014

Notes: End-member mole fractions are calculated as: [Na/(Ca + Na + K)]= Ab; [Ca/(Ca + Na + K)]= An; and [K/(Ca + Na + K)]= Or. Mineral abbreviations from Kretz (1983).

Table 3. Representative microprobe analyses and calculated formula of biotite (single spots).

Rock type:	Staurolite-bearing high-grade schist					Corundum-bearing schist			Gneiss		Granite
Sample:	976B-74X-1, 30-34 cm	76R-1, 03-07 cm	74X-1, 30-34 cm	76R-1, 45-49 cm	76R-1, 03-07 cm	77R-2, 24-26 cm	77R-2, 40-42 cm	77R-2, 24-26 cm	98R-1, 38-40 cm	98R-1, 38-40 cm	82R-1, 93-98 cm
Textural position:	Matrix	Matrix	Rim garnet	Included garnet II	Included plagioclase	Matrix	Matrix	Included Pl	Matrix	Matrix	Matrix
Analytic point:	B-24	D-11	C-29	B-103	B-44	E-15	F-27	B-23	9	13	A-2
SiO_2	34.94	34.55	34.55	33.81	33.38	34.13	35.81	34.41	34.13	33.95	35.19
Al_2O_3	20.68	20.84	19.57	18.23	19.81	20.73	18.70	19.30	19.12	19.99	19.69
TiO_2	2.84	3.62	3.44	3.70	3.86	2.27	1.42	4.38	2.35	3.34	3.36
MgO	4.68	2.92	5.19	4.10	3.51	4.92	8.87	4.61	4.89	4.55	5.32
FeO	23.09	23.45	22.99	25.96	24.55	23.47	20.56	23.06	25.30	24.20	21.75
MnO	0.23	0.12	0.24	0.20	0.10	0.24	0.24	0.24	0.30	0.40	0.35
CaO	0.02	0.02	0.00	0.02	0.03	0.01	0.02	0.02	0.00	0.00	0.00
Na_2O	0.18	0.12	0.09	0.19	0.16	0.11	0.15	0.17	0.15	0.13	0.08
K_2O	8.77	9.27	9.07	8.66	9.15	8.82	9.12	9.16	9.08	9.03	8.98
Total	95.43	94.91	95.14	94.87	94.55	94.70	94.89	95.35	95.32	95.59	94.71
Cations normalized to 22 oxygens (all Fe as Fe^{2+})											
Si	5.374	5.367	5.352	5.346	5.257	5.313	5.492	5.330	5.352	5.278	5.433
Al^{iv}	2.626	2.633	2.648	2.654	2.743	2.687	2.508	2.670	2.648	2.722	2.567
Sum Z	8.000	8.000	8.000	8.000	8.000	8.000	8.000	8.000	8.000	8.000	8.000
Al^{vi}	1.124	1.185	0.926	0.743	0.936	1.117	0.872	0.855	0.886	0.941	1.016
Ti	0.328	0.423	0.401	0.440	0.457	0.266	0.164	0.510	0.278	0.391	0.391
Mg	1.072	0.676	1.199	0.967	0.823	1.141	2.027	1.064	1.142	1.054	1.224
Fe^{2+}	2.970	3.046	2.978	3.432	3.234	3.055	2.636	2.987	3.318	3.146	2.807
Mn	0.030	0.016	0.032	0.027	0.014	0.032	0.032	0.031	0.039	0.053	0.045
Sum Y	5.524	5.346	5.536	5.609	5.464	5.611	5.731	5.447	5.663	5.585	5.483
Ca	0.004	0.003	0.001	0.003	0.004	0.001	0.003	0.004	0.000	0.000	0.000
Na	0.055	0.036	0.027	0.058	0.049	0.034	0.046	0.050	0.045	0.039	0.023
K	1.721	1.837	1.792	1.746	1.838	1.751	1.785	1.810	1.816	1.791	1.768
Sum X	1.780	1.876	1.820	1.807	1.891	1.786	1.834	1.864	1.861	1.830	1.791

domains is closer to phlogopite compositions (mg# ~ 0.4–0.5). This difference indicates that biotite grew during two separate metamorphic stages.

High Ti content characterizes biotite grains in all the rock types (0.3–0.45 ions pfu), with the exception of corundum-bearing metapelites, where biotite has low Ti content (< 0.2 ions pfu). $Al^{[vi]}$ content varies widely from staurolite-bearing schist (0.70–1.1 ions pfu) to gneissic rocks (0.79–1.0 ions pfu), and granite rocks (0.86–1.34 ions pfu). Mg content increases in biotite from banded gneiss and pelitic domains in migmatite gneiss (1.0–1.75 ions pfu; mg# =

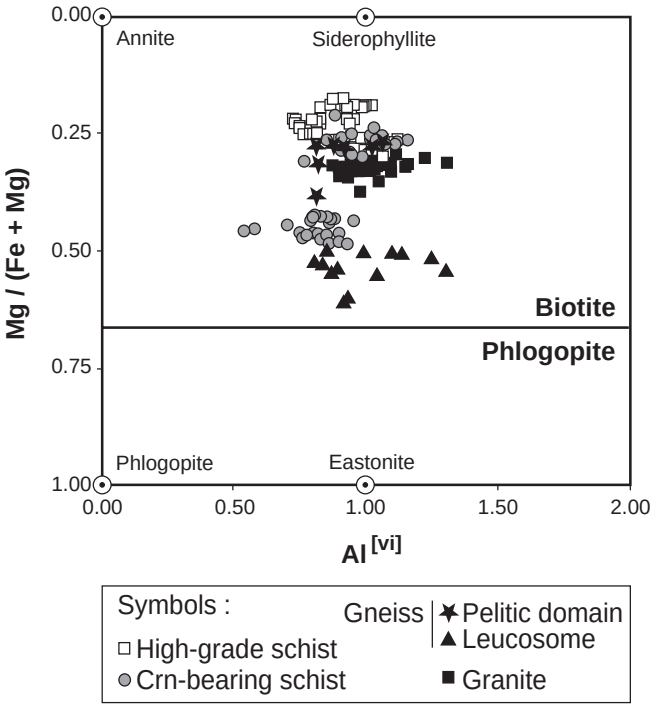

Figure 6. Selected biotite compositions are plotted in the "ideal biotite plane" diagram of Guidotti (1984). Biotite end-members are shown for comparison. Arbitrary division between phlogopites and biotites (Mg:Fe = 2:1) are taken from Deer et al. (1966).

0.27–0.37); to leucosome veins (>2.25 ions pfu; mg# = 0.49–0.61). Biotite from high-grade schists has low Mg content in any textural position (0.75–1.25 ions pfu; mg# = 0.16–0.25).

In conclusion, matrix porphyroblasts in all the rock types show a homogeneous composition largely controlled by bulk-rock chemistry variations, apart from those biotite grains close to destabilization minerals (e.g., garnet, staurolite, cordierite, etc.).

Staurolite

Staurolite has a little chemical variation in Fe, which is higher in matrix porphyroblasts (2.9–3.1 ions pfu) than in relict grains included in andalusite (2.6–2.8 ions pfu; Table 4). Mg and Zn contents are always very low (<0.2 ions pfu and <0.17, respectively). Relict inclusions of staurolite in garnet II from the high-grade schist usually have a typical increase of the Mg:Fe ratio with respect to matrix porphyroblasts. This variation suggests that these staurolite grains are involved in the garnet-forming reactions.

Staurolite is partially transformed to hercynite ($Hc_{0.9}$ $Spl_{0.1}$; Table 4) inside andalusite porphyroblasts and to ilmenite and pyrite in the matrix.

Cordierite

Cordierite, either as relict or partially pinnitized grains porphyroblasts in the matrix, has a constant chemical composition, with Mg/(Mg + Fe + Mn) values between 0.6 and 0.7 (Table 4). The total amount of oxides in nontransformed cordierite grains (98–98.5 wt%) suggests that this mineral could have up to 1.5–2.0 wt% H_2O.

Ti-Fe Oxides

Magnetite and Ti-magnetite are present exclusively in gneissic rocks (Table 4). The latter is preserved only inside biotite porphyroblasts. The presence of Ti-magnetite has been previously reported in other high-grade rocks (see Rumble, 1976), as this mineral is restricted to temperatures higher than 600°C (Lindsley, 1976). (Although the term Ti-magnetite should be restricted to those specimens where an ulvöspinel phase can be demonstrated by X-ray analysis [Deer et al., 1966], we have used this term to indicate the occurrence of a significant Ti = Fe^{3+} substitution in magnetite.)

PRESSURE-TEMPERATURE CONDITIONS

To reconstruct the PT evolution of basement rocks, we first need to determine the paragenetic sequence in the high-grade schist and gneiss. After that, we can apply geothermometers and geobarometers. The results help place useful constraints on the PT history of these rocks, but also demonstrate that in most cases the minerals are not in equilibrium.

Interpretation of the Paragenetic Sequence

High-Grade Schist

In the high-grade schist, we can identify an early post-S_1 to S_2 assemblage of quartz + biotite + garnet I + staurolite + plagioclase + Ti-Fe oxide (assemblage 1). Given the bulk composition of the schist, muscovite was almost certainly present, but is not now preserved. In the KFMASH system (K_2O-FeO-MgO-Al_2O_3-SiO_2-H_2O), assemblage 1 corresponds to a divariant assemblage Grt + St + Bt + muscovite (Ms; Fig. 7), and it is therefore unlikely that an aluminosilicate was present in equilibrium with this assemblage (see Spear and Cheney, 1989).

The normal zoning pattern of garnet I suggests prograde metamorphism with increasing temperature and/or decreasing pressure, but the timing of this garnet growth is not clear from textural evidence. Resorption of garnet I may have occurred either as a result of the prograde univariant reaction Grt + Chl + Ms = St + Bt + Qtz + H_2O, or during decompression, by the net transfer reaction Grt + Ms + H_2O = St + Bt + Qtz, before staurolite had become unstable.

During D_2, the stable assemblage in the high-grade schist is probably quartz + biotite + sillimanite + K-feldspar + ilmenite (assemblage 2). Staurolite became unstable when the conditions surpassed the univariant reaction St + Ms + Qtz = Grt + Bt + Sil + H_2O, and muscovite breakdown occurred because of the dehydration melting reaction Ms + Pl + Qtz = Kfs + aluminosilicate (Als) + L (melt) (Fig. 7A). Textural evidence that support both reactions are the preservation of relict staurolite inside garnet II porphyroblasts, and the presence of K-feldspar + plagioclase + quartz intergrowths included in garnet II together with K-feldspar + plagioclase including blebs of andalusite. The latter two textures are interpreted as resulting from the later crystallization of residual melts, formed by the above-mentioned muscovite-dehydration melting reaction. Therefore, assemblage 2 results from the overstepping of two divariant assemblages in the KFMASH system, Grt + Bt + Sil + Ms and Grt + Bt + Sil + Kfs. Taken all together, this sequence indicates decompression, accompanied by constant or increasing T. Barometric estimates will provide additional evidences for decompression during D_2.

Textural evidence suggests that the latest growth of garnet II occurs after D_2, and therefore at lower P and/or higher T than the muscovite breakdown reaction. Garnet growth at this stage would involve staurolite breakdown under overstepped conditions, as suggested by the fact that some garnet II grains include corroded staurolite relics and include K-feldspar + plagioclase intergrowths. The only other

Table 4. Representative microprobe analyses of staurolite, spinel, cordierite, and Ti-Fe oxides (single spots).

Mineral:	Spinel	Staurolite	Magnetite	Ilmenite	Cordierite
Rock type:	St-HGS	St-HGS	Gneiss	St-HGS	Gneiss
Sample:	976B-74X-1, 30-34 cm	76R-1, 45-49 cm	98R-1, 96-101 cm	76R-1, 03-07 cm	95R-2, 24-28 cm
Textural position:	Included in andalusite	Matrix	Matrix	Included in andalusite	Rim
Analytic point:	A-22	C-3	84d	C-24	5-per 1
SiO_2	3.37	27.24	0.02	0.03	48.64
Al_2O_3	57.05	55.92	0.42	0.06	32.43
TiO_2	0.11	0.47	0.17	52.29	0.01
Cr_2O_3	0.24	0.07	0.03	0.04	0.02
MgO	1.90	0.59	0.00	0.02	9.09
FeO	30.41	13.45	45.61	43.84	6.71
Fe_2O_3 (Δ)	—	0.54	50.56	0.00	—
MnO	0.48	0.24	0.04	2.30	0.35
ZnO	0.00	0.23	0.00	0.00	n.d.
CaO	n.d.	n.d.	n.d.	n.d.	0.02
Na_2O	n.d.	n.d.	n.d.	n.d.	0.29
K_2O	n.d.	n.d.	n.d.	n.d.	0.01
H_2O (#)	—	3.35	—	—	—
Total ($-H_2O$)	93.55	98.75	96.85	98.60	97.55
Cations normalized to 32 oxygens (Mag, Spl), 6 oxygens (Ilm), 46.5 oxygens (St)					
Si	0.788	7.271	0.006	0.002	5.020
Al	15.737	17.594	0.206	0.004	3.944
Ti	0.019	0.095	0.053	2.007	0.001
Cr	0.044	0.014	0.009	0.002	0.002
Fe^{3+} (Δ)	0.000	0.109	7.874	0.000	—
Σ[B], $[Al]^{vi}$	16.589	17.082	8.149	2.014	8.967
Mg	0.663	0.233	0.000	0.002	1.398
Fe^{2+}	5.955	3.002	15.787	1.873	0.579
Mn	0.094	0.054	0.015	0.099	0.030
Zn	0.000	0.044	0.000	0.000	n.d.
Σ[A], $[Fe]^{vi}$	6.713	3.334	15.802	1.974	2.007
Ca	n.d.	n.d.	n.d.	n.d.	0.002
Na	n.d.	n.d.	n.d.	n.d.	0.058
K	n.d.	n.d.	n.d.	n.d.	0.001
Σ total Cat	23.302	28.416	23.952	3.988	11.036

Spinel	9.882	Li	0.200	X Mg	0.697	
Hercynite	88.715	H	5.919	Σ CC	0.062	
Galaxite	1.403	XMg	0.071			
Gahnite	0.000	XFe	0.915			
		XZn	0.014			

Notes: End-member fractions of spinel are calculated as (100 × Mg/Σ[A]) = spinel; (100 × Fe/Σ[A]) = hercynite; (100 × Mn/Σ[A]) = galaxite; and (100 × Zn/Σ[A]) = gahnite. Li and H contents are determined by the staurolite-normalization procedure (Hawthorne et al., 1993) (46.5 Ox; Li = 0.2 and H = 3.06 apfu; Fe^{3+} = 3.5 wt% total Fe). Subsequently, H_2O (#) and Fe_2O_3 (Δ) are back-calculated. For the other minerals, Fe^{3+} contents (Δ) are calculated as described by Droop (1987). X Mg = Mg/(Mg + Mn + Fe^{2+}) and CC= Σ (Ca + Na + K) in cordierite. St-HGS = Staurolite-bearing high-grade schist. Mineral abbreviations are from Kretz (1983); n.d. = not determined; **—** = not calculated.

garnet-forming reaction that could have been involved is the breakdown of biotite by the reaction Bt + Sil = Grt + Crd (Fig. 7A), which is ruled out by the absence of cordierite in the high-grade schist.

The final assemblage in these rocks is quartz + biotite + andalusite + K-feldspar + plagioclase + ilmenite (assemblage 3). This assemblage is interpreted to be formed by crystallization of residual melts in the andalusite stability field.

Pelitic and Migmatite Gneiss

In the gneiss, the present assemblage is quartz + biotite + muscovite + sillimanite + andalusite + cordierite + plagioclase + K-feldspar + ilmenite ± garnet. This is clearly not an equilibrium assemblage, but the textural relationships do not allow an unequivocal paragenetic sequence to be established. Rather, the gneiss is best interpreted as a disequilibrium assemblage resulting from a series of strongly overstepped reactions that did not continue to completion.

The fibrolite seams probably reflect the result of the muscovite breakdown reaction (Ms + Qtz = L + Kfs + Sil or Ms + Pl + Qtz = L + Kfs + Als; Fig. 7B), leaving the assemblage Qtz + Bt + Sil + Kfs + Pl. The next step seems to have involved the partial breakdown of biotite, probably by a melting reaction that produced abundant Fe-Ti oxide (e.g., Bt + Sil = Grt + Spl + Mag + L; Clarke et al., 1989). Locally, garnet was probably produced by this reaction.

Textural observations support a final growth of cordierite, K-feldspar, and andalusite, probably representing the final crystallization of granitic melts. Large cordierite phenocrysts also occur with biotite and fibrolite inclusions. This textural evidence suggests a continuous growth of cordierite accompanying the melting reactions, and a final crystallization of melts in the andalusite stability field forming aggregates of cordierite, K-feldspar, and new biotite phenocrysts.

The observed disappearance of garnet I porphyroblasts, coupled with the appearance of cordierite in these rocks, suggests that cordierite could be partially formed by garnet-consuming reactions, such as Sil + Grt + Qtz + H_2O = Crd (Fig. 7B). Continued growth of cordierite could be related to melting reactions, such as: Bt + Als + Qtz = L + Crd + Kfs (Fig. 7B).

The melt crystallization also produced new, Al-rich biotite, from the reaction L = Al-rich-Bt + Crd + Kfs + Qtz + H_2O (Vielzeuf and Holloway, 1988; Fig. 7B). The coexistence of andalusite and a granitic melt can be explained by considering the expansion of the PT melt field because of the addition of B, F, and excess Al (see the summary in Johannes and Holtz, 1996). In view of the presence of tourmaline and monazite in the gneissic rocks, together with the Als + Pl-rich composition of leucosome veins, it is likely that the granite solidus in the rocks was displaced toward lower temperatures, within the andalusite stability field at low pressures (Fig. 7B).

The final stage in the evolution of the gneiss was growth of muscovite, perhaps because of the reaction between a residual hydrous

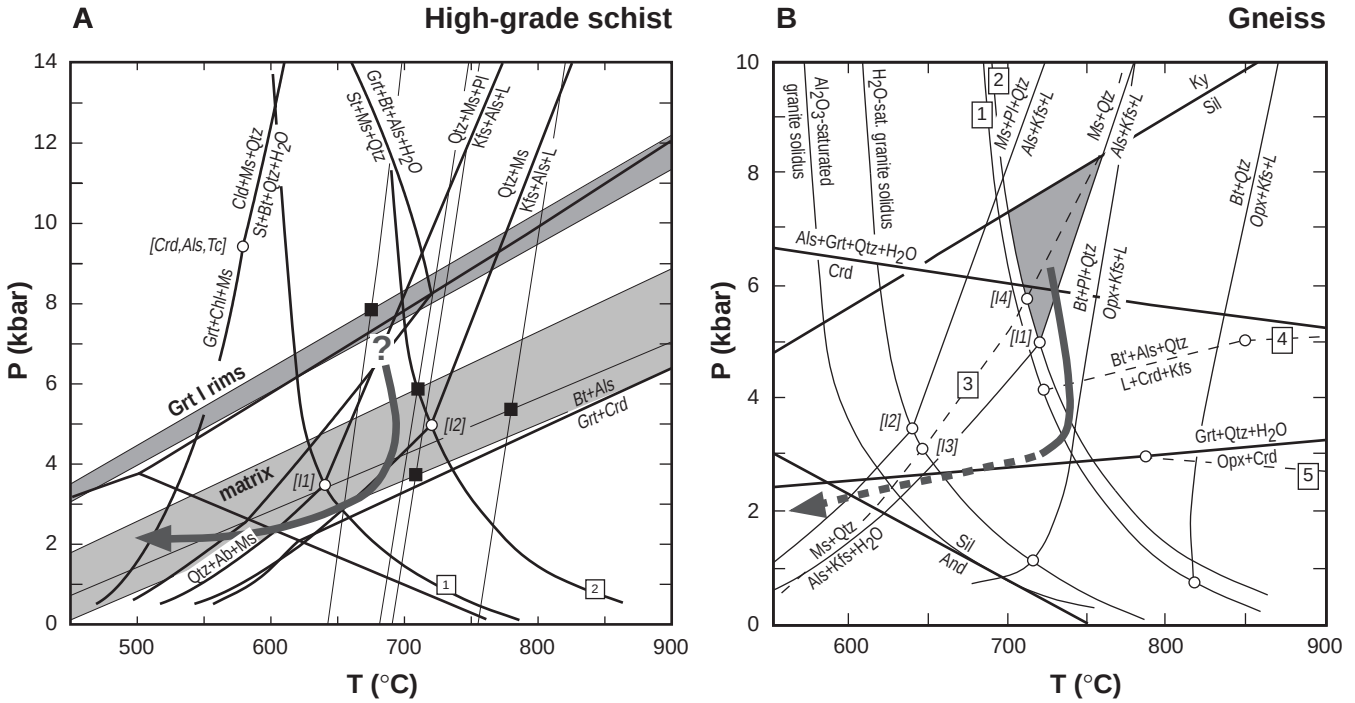

Figure 7. **A.** PT paths followed by high-grade schist. PT plots of selected thermobarometric results per sample (thin lines) and approximate PT evolution during and after (thick arrow) D_2 of the high-grade schist. Black squares represent simultaneous intersection between garnet-biotite thermometer (Hodges and Spear, 1982) and GASP barometer (Hodges and Crowley, 1985). P conditions for plagioclase included in garnet porphyroblasts (dark gray) and garnet-plagioclase rims in the matrix (light gray) are shown for reference. Thick lines represent key reactions in KFMASH system (Spear and Cheney, 1989). Invariant points [I1] and [I2] represent Pl-bearing (i.e., in KNASH system) and Pl-absent (i.e., in KASH system) invariant points, respectively, for the muscovite-melting reaction. Granite solidus is represented by reaction 1 (in the Qtz-Ab-Or-H_2O system; Ms + Ab + Bt + Kfs + Qtz + H_2O = L; which under [I1] is transformed to Kfs + Als + Bt + Qtz + H_2O = L) and reaction 2 (in the Qtz-Or-H_2O subystem; Ms + Bt + Kfs + Qtz + H_2O = L; which under [I2] is transformed to Kfs + Als + Bt + Qtz + H_2O = L). **B.** PT evolution of the pelitic and migmatite gneiss (thick arrow). The cooling path is indicated by the broken line. Dark gray area represents the deduced PT conditions for the first stages of melting (see text). Selected reactions in the KFMASH system are taken from Vielzeuf and Holloway (1988; X_{Mg} ~ 0.5); dashed lines represent reactions involving Al-rich micas (Al-rich biotite: Bt′, $[Al]^{vi}$ = 1.0; and Al-rich muscovite: Ms′, $Si:Al^{iv}$ > 3:1). Other melting reactions are from Vielzeuf and Clemens (1992). Data sources for granite solidi are summarized in Johannes and Holtz (1996). Reactions (right term points to the higher temperature side of the reaction) 1: Bt + Kfs + Qtz + H_2O = L; 2: Ms + Kfs + Qtz + H_2O = L which under [I1] is transformed to Als + Kfs + Qtz + H_2O = L; 3: under [I3] is Ms′ + Qtz = Crd + Kfs + Als + H_2O, between [I3] and [I4] is Ms′ + Qtz = Bt′ + Kfs + Als + H_2O, and above [I4] is Ms′ + Qtz = L + Kfs + Als + Bt′; 4: L + Grt + Als + Qtz = Crd + Kfs; 5: Bt′ + Crd + Opx = L + Grt + Opx. Notice that the location of the divariant reactions Als + Grt + Qtz + H_2O = Crd and Grt + Qtz + H_2O = Opx + Crd (thick lines in the diagram) depends on the X_{Mg} contents of the phases. We have represented for comparison the location of both reactions for a fixed composition of X_{Mg} ~ 0.5 (from Vielzeuf and Holloway, 1988). Al-silicate triple point is from Berman (1988).

fluid and the aluminous phases in the rock: Crd + Kfs + Als + H_2O = Ms + Qtz and Kfs + Als + H_2O = Ms + Qtz (Fig. 7B).

Quantitative PT Determinations: the PT Path

To determine the PT conditions achieved by the basement rocks we have applied different geothermometers and geobarometers. In order to avoid internal discrepancies in consistency between different calibrations, we have selected those using the same thermodynamic database.

High-Grade Schist

Application of the garnet-Al-silicate-plagioclase (GASP) barometer (Hodges and Crowley, 1985) to plagioclase inclusions in garnet consistently gives slightly higher pressures in garnet I inner rims than in garnet II, which reflects in part the decreasing grossular component toward the rims. For an assumed temperature of 700°C, the calculated pressures are between 8.5 and 7.5 kbar, close to the kyanite-sillimanite transition (Fig. 7A). The garnet-plagioclase rims formed under lower pressures, but over a large pressure-range (3.5–5.5 kbar at 700°C). A similar pressure range is also obtained by using the garnet-plagioclase-biotite-quartz (GPBQ) barometer of Hoisch (1990). Pressure estimates using the GASP geobarometer for garnet I rims should be considered as maximum values, because of the lack of an Al-silicate in equilibrium with assemblage 1.

Garnet-biotite (GARB) thermometry (Hodges and Spear, 1982), applied to garnet-biotite rims in the matrix, gives us a wide variation in temperatures, from 650° to 850°C (at an estimated pressure of 4 kbar; Fig. 7A). The wide span in the calculated temperature (some incompatible with the stability field of the observed mineral assemblage) is further evidence of disequilibrium in these rocks (see García-Casco and Torres-Roldán, 1996). Another important factor to consider is that garnet homogenization by diffusion is enhanced by the high-grade conditions. This has occurred in some garnet rims and, therefore, these calculated temperatures should be used with caution. Many authors have also questioned the use of this geothermometer in high-grade rocks (e.g., Selverstone and Chamberlain, 1990; Spear and Florence, 1992). It is quite clear that the textural evidence (e.g., dissolution of garnet exposed different rim compositions, garnet is partially consumed by biotite in the matrix, diffusion processes, etc.), as well as the variability of the results, indicate that the GARB esti-

mates are not reliable in these rocks. Therefore, the temperatures must be constrained by phase assemblages. Considering that the stable assemblage during D_2 (assemblage 2: Sil + Kfs + Bt + Ilm) in the high-grade schist results from staurolite and muscovite dehydration melting reaction, we suggest that peak temperatures in these rocks during D_2 were in the range of 650° to 700°C (Fig. 7A).

Keeping in mind these constraints, and taking the GARB estimates together with the results of the GASP and GPBQ barometers, we estimate approximate PT conditions of 8.5–7.5 kbar for garnet I rims and 3.5–5.5 kbar at 650°–700°C for the matrix S_2 assemblage in the high-grade schist. Temperature estimates for garnet I rims could not be defined with the data presented in this paper, although phase relation modeling based on garnet I zoning patterns will help constrain the PT conditions and reaction history these rocks underwent at this stage (Soto and Platt, in press).

In spite of difficulties inherent to disequilibrium problems (spurious GARB results, overstepping reactions, etc.) we can propose an approximate and partial PT path for the high-grade schist during D_2 and afterward. We have documented a limited drop in P during D_2 (from maximum pressures of 8.5–7.5 to 3.5–5.5 kbar), achieving T between invariant points [I1] and [I2] at low P (Fig. 7A). The decompression PT path during D_2 occurred probably under increasing T conditions, as documented by Soto and Platt (in press).

After D_2, the rocks underwent a sharp temperature drop at low P (3–2 kbar). Metastable survival of early phases developed under higher pressure and temperature conditions (e.g., staurolite, garnet I without garnet II rims), together with the reconstruction of strongly overstepped reactions (e.g., staurolite preserved in andalusite), suggest that the cooling portion of the PT path proceeded probably at a very fast rate, which is also supported by age determinations in these rocks (see Kelley and Platt, Chap. 22, this volume; Monié et al., 1994).

Gneiss

Standard geothermometers and geobarometers (e.g., garnet-cordierite) in gneissic rocks always give spurious results. This result confirms our hypothesis that many of the mineral assemblages in the gneissic rocks are not in equilibrium. Any work on these rocks to determine the PT path should be done using available petrogenetic grids, and therefore the results should be considered qualitative. To account for melting reactions in metapelitic rocks, we have used the experimentally derived grid of Vielzeuf and Holloway (1988) in the KFMASH system (fluid-absent grid, $X_{Mg} = 0.5$) and other dehydration melting reactions derived by Vielzeuf and Clemens (1992; Fig. 7B).

Textural evidence suggests that melting occurred in these rocks because of the muscovite and biotite breakdown reactions. Muscovite dehydration melting reactions occur at pressures <4–5 kbar and temperatures >700°C (Fig. 7B). The intersection between the Ms-out reaction without plagioclase (reaction Ms + Qtz = Als + Kfs + L; Fig. 7B) and the granite melting curve defines an invariant point [I1] placed at ~725°C-5 kbar. Consequently, to form the granitic assemblage Qtz + Bt + Sil + Kfs + Pl, the gneissic rocks must surpass the band of reactions that define the Ms-out melting curve (dark gray area in Fig. 7B) at temperatures between the invariant point [I1] and those at the reactions involving melting of biotite to form pyroxene (Bt + Pl + Qtz = Opx + Kfs + L); that is, at T = 700°–750°C. P conditions for this assemblage are constrained by the presence of cordierite accompanying melting (i.e., P < 4–4.5 kbar; limit defined by the reaction Bt + Als + Qtz = L + Crd + Kfs).

All these observations together suggest a decompression PT path for the gneiss, at 700°–750°C, from at least 6 kbar to 3 kbar. Melting occurred along the decompression path by successive breakdown of muscovite and biotite. Cordierite was stable during melting, although its major growth occurred at low-P conditions, at the expense of biotite.

The decompression PT path was followed by a cooling path (P < 3 kbar) up to the andalusite stability field (T ~ 600°C). During this portion of the path, crystallization of residual melts occurred. These melts formed muscovite, new biotite (different in composition to restitic biotite), together with K-feldspar, plagioclase, cordierite, quartz, and andalusite. We interpret that a large overstepping of reactions occurred during the cooling path, resulting in complex textural relationships between these minerals. In particular, andalusite formed either as inclusions or including minerals of the granitic assemblage (Kfs + Pl + Crd). The contradictory textural relationships for andalusite in these rocks were previously interpreted as a result of heating under very low P conditions (Platt et al., 1996). Nevertheless, a careful textural interpretation of a more complete set of samples, together with the chemical characterization of the phases, allows us to reinterpret the PT path followed by these rocks.

CONCLUSIONS

The continental basement of the Alboran Sea basin at Site 976 (Holes 976B and 976E) has undergone decompression during the development of the most conspicuous fabric (foliation S_2) in the rocks. This is observed in two distinctive PT paths for the high-grade schist and the gneiss during D_2, followed by a nearly isobaric cooling path. We have documented misleading thermobarometric estimates because of the widespread occurrence of disequilibrium assemblages. Based on phase relationships and critical use of the geothermobarometric data, we suggest that the decompression path occurred at least from 8–7 to 3 kbar at 650°–700°C in the high-grade schist, and from 5 to 3 kbar at 700°–750°C in the gneiss. These PT conditions are similar to those obtained in the Alpujárride units underlying the Ronda peridotite slab in the Western Betic Cordillera (see revision in Sánchez-Gómez et al., Chap. 23, this volume). After decompression, cooling was near isobaric (P < 3 kbar), which led to a probably rapid crystallization of residual melts within the andalusite stability field (T ~ 600°C).

ACKNOWLEDGMENTS

J.I. Soto would like to thank ODP for inviting him to participate in Leg 161. We would also like to thank the Shipboard Scientific Party, the ODP technicians, and the SEDCO drilling crew of Leg 161 for their help, and Menchu Comas, one of the Co-Chief Scientists, for her support. This paper has benefited from the thorough revisions done by Ian Fitzsimons and Virginia Sisson. J.I. Soto acknowledges financial support provided by Project AMB95-1557-CICYT. J.P. Platt acknowledges grant number GR3/10828 from the Natural Environmental Research Council of Great Britain.

REFERENCES

Berman, R.G., 1988. Internally consistent thermodynamic data for minerals in the system Na_2O-K_2O-CaO-MgO-FeO-Fe_2O_3-Al_2O_3-SiO_2-TiO_2-H_2O-CO_2. *J. Petrol.*, 292:445–522.

Buntfuss, J., 1970. Die Geologie der Kuestenketten zwischen dem Rio Verde und dem Campo de Gibraltar (Westliche Betische Kordillere/Südspanien). *Geol. Jahrb.*, 88:373–420.

Clarke, G.L., Powell, R., and Guiraud, M., 1989. Low-pressure granulite facies metapelitic assemblages and corona textures from MacRobertson Land, east Antarctica: the importance of Fe_2O_3 and TiO_2 in accounting for spinel-bearing assemblages. *J. Metamorph. Geol.*, 7:323–335.

Comas, M.C., García-Dueñas, V., and Jurado, M.J., 1992. Neogene tectonic evolution of the Alboran Basin from MCS data. *Geo-Mar. Lett.*, 12:157–164.

Comas, M.C., García-Dueñas, V., Soto, J.I., and Campos, J., 1993. An extensional basin developed on a collisional orogen: the Alborán Sea. *In* Seranne, M., and Malavielle, J. (Eds.), *Late Orogenic Extension in Mountain Belts.* Doc. B.R.G.M. Fr., 219:44–46.

Comas, M.C., Zahn, R., Klaus, A., et al., 1996. *Proc. ODP, Init. Repts.*, 161: College Station, TX (Ocean Drilling Program).

Deer, W.A., Howie, R.A., and Zussman, J., 1966. *An Introduction to the Rock-Forming Minerals:* London (Longman Group).

de la Linde, J., Comas, M.C., and Soto, J.I., 1996. Morfología del basamento en el nor-oeste del Mar de Alborán. *Geogaceta*, 20:355–358.

Droop, G.T.R., 1987. A general equation for estimating Fe^{3+} concentrations in ferromagnesian silicates and oxides from microprobe analyses, using stoichiometric criteria. *Mineral. Mag.*, 51:431–435.

García-Casco, A., and Torres-Roldán, R.L., 1996. Disequilibrium induced by fast decompression in St-Bt-Grt-Ky-Sil-And metapelites from the Betic Belt (Southern Spain). *J. Petrol.*, 37:1207–1239.

García-Dueñas, V., Balanyá, J.C., and Martínez-Martínez, J.M., 1992. Miocene extensional detachments in the outcropping basement of the northern Alboran basin (Betics) and their tectonic implications. *Geo-Mar. Lett.*, 12:88–95.

Guidotti, C.V., 1984. Micas in metamorphic rocks. *In* Bailey, S.W. (Ed.), *Micas.* Mineral. Soc. Am., Rev. Mineral., 13:357–468.

Hawthorne, F.C., Ungaretti, L., Oberti, R., Caucia, F., and Callegari, A., 1993. The crystal chemistry of staurolite. I. Crystal structure and site populations. *Can. Mineral.*, 31:551–582.

Hodges, K.V., and Crowley, P.D., 1985. Error estimation and empirical geothermobarometry for pelitic systems. *Am. Mineral.*, 60:702–709.

Hodges, K.V., and Spear, F.S., 1982. Geothermometry, geobarometry and the Al_2SiO_5 triple point at Mt. Moosilauke, New Hampshire. *Am. Mineral.*, 67:1118–1134.

Hoisch, T.D., 1990. Empirical calibration of six geobarometers for the mineral assemblage quartz + muscovite + biotite + plagioclase + garnet. *Contrib. Mineral. Petrol.*, 104:225–234.

Johannes, W., and Holtz, F., 1996. *Petrogenesis and Experimental Petrology of Granitic Rocks:* Berlin (Springer-Verlag).

Kerrick, D.M., and Speer, J.A., 1988. The role of minor element solid solution on the andalusite-sillimanite equilibrium in metapelites and peraluminous granitoids. *Am. J. Sci.*, 288:152–192.

Kretz, R., 1983. Symbols for rock-forming minerals. *Am. Mineral.*, 68:277–279.

Lindsley, D.H., 1976. Experimental studies of oxide minerals. *In* El Goresy, A., Haggerty, S.E., Huebner, J.S., Lindsley, D.H., and Rumble, D., III (Eds.), *Oxide Minerals.* Mineral. Soc. Am., Short Course Notes, 3:61–88.

Loomis, T.P., 1972. Contact metamorphism of pelitic rocks by the Ronda ultramafic intrusion, southern Spain. *Geol. Soc. Am. Bull.*, 83:2449–2474.

Lundeen, M.T., 1978. Emplacement of the Ronda peridotite, Sierra Bermeja, Spain. *Geol. Soc. Am. Bull.*, 89:172–180.

McLellan, E.L., 1983. Contrasting textures in metamorphic and anatectic migmatites: an example from the Scottish Caledonides. *J. Metamorph. Geol.*, 1:339–345.

Mehnert, K.R., 1968. *Migmatites and the Origin of Granitic Rocks:* New York (Elsevier).

Mollat, H., 1968. Schichtenfolge und tektonischer Bau der Sierra Blanca und ihrer Umgebung (Betische Kordilleren, Südspanien). *Geol. Jahrb.*, 86:471–482.

Monié, P., Torres-Roldán, R.L., and García-Casco, A., 1994. Cooling and exhumation of the western Betic Cordilleras, $^{40}Ar/^{39}Ar$ thermochronological constraints on a collapsed terrane. *Tectonophysics*, 238:353–379.

Platt, J.P., and Vissers, R.L.M., 1989. Extensional collapse of thickened continental lithosphere: a working hypothesis for the Alboran Sea and Gibraltar Arc. *Geology*, 17:540–543.

Platt, J.P., Soto, J.I., Comas, M.C., and Leg 161 Shipboard Scientific Party, 1996. Decompression and high-temperature–low-pressure metamorphism in the exhumed floor of an extensional basin, Alboran Sea, Western Mediterranean. *Geology*, 24:447–450.

Pouchou, J.L., and Pichoir, F., 1985. PAP $\phi(\rho z)$ procedure for improved quantitative microanalysis. *In* Armstrong, J.T. (Ed.), *Microbeam Analysis:* (San Francisco Press), 104–106.

Rumble, D., III, 1976. Oxide minerals in metamorphic rocks. *In* El Goresy, A., Haggerty, S.E., Huebner, J.S., Lindsley, D.H., and Rumble, D., III (Eds.), *Oxide Minerals.* Mineral. Soc. Am., Short Course Notes, 3:1–24.

Ryan, W.B.F., Hsü, K.J., et al., 1973. *Init. Repts. DSDP*, 13 (Pts. 1 and 2): Washington (U.S. Govt. Printing Office).

Sánchez-Gómez, M., García-Dueñas, V., and Muñoz, M., 1995. Relations structurales entre les Péridotites de la Sierra Bermeja et les unités alpujarrides sous-jacentes (Benahavís, Ronda, Espagne). *C. R. Acad. Sci. Paris*, 321:885–892.

Selverstone, J., and Chamberlain, C.P., 1990. Apparent isobaric cooling paths from granulites: two counterexamples from British Columbia and New Hampshire. *Geology*, 18:307–310.

Shipboard Scientific Party, 1996. Site 976. *In* Comas, M.C., Zahn, R., Klaus, A., et al., *Proc. ODP, Init. Repts.*, 161: College Station, TX (Ocean Drilling Program), 179–297.

Soto, J.I., Comas, M.C., and de la Linde, J., 1996. Espesor de sedimentos en la cuenca de Alborán mediante una conversión sísmica corregida. *Geogaceta*, 20:382–385.

Soto, J.I., and Platt, J.P., in press. Petrological and structural evolution of high-grade metamorphic rocks from the Alboran Sea Basin, W. Mediterranean. *J. Petrol.*

Spear, F.S., and Cheney, J.T., 1989. A petrogenetic grid for pelitic schists in the system SiO_2-Al_2O_3-FeO-MgO-K_2O-H_2O. *Contrib. Mineral. Petrol.*, 101:149–164.

Spear, F.S., and Florence, F.P., 1992. Thermobarometry in granulites: pitfalls and new approaches. *J. Precambrian Res.*, 55:209–241.

Vernon, R.H., 1986. K-feldspar megacrysts in granites—phenocrysts, not porphyroblasts. *Earth-Sci. Rev.*, 23:1–63.

Vernon, R.H., and Flood, R.H., 1977. Interpretation of metamorphic assemblages containing fibrolitic sillimanite. *Contrib. Mineral. Petrol.*, 59:227–235.

Vielzeuf, D., and Clemens, J.D., 1992. The fluid-absent melting of phlogopite + quartz: experiments and models. *Am. Mineral.*, 77:1206–1222.

Vielzeuf, D., and Holloway, J.R., 1988. Experimental determination of the fluid-absent melting relations in the pelitic system: consequences for crustal differentiation. *Contrib. Mineral. Petrol.*, 98:257–276.

Watts, A.B., Platt, J.P., and Buhl, P., 1993. Tectonic evolution of the Alboran Sea Basin. *Basin Res.*, 5:153–177.

Westerhof, A.B., 1977. On the contact relations of high-temperature peridotites in the Serrania de Ronda, southern Spain. *Tectonophysics*, 39:579–591.

Date of initial receipt: 7 May 1997
Date of acceptance: 6 November 1997
Ms 161SR-218

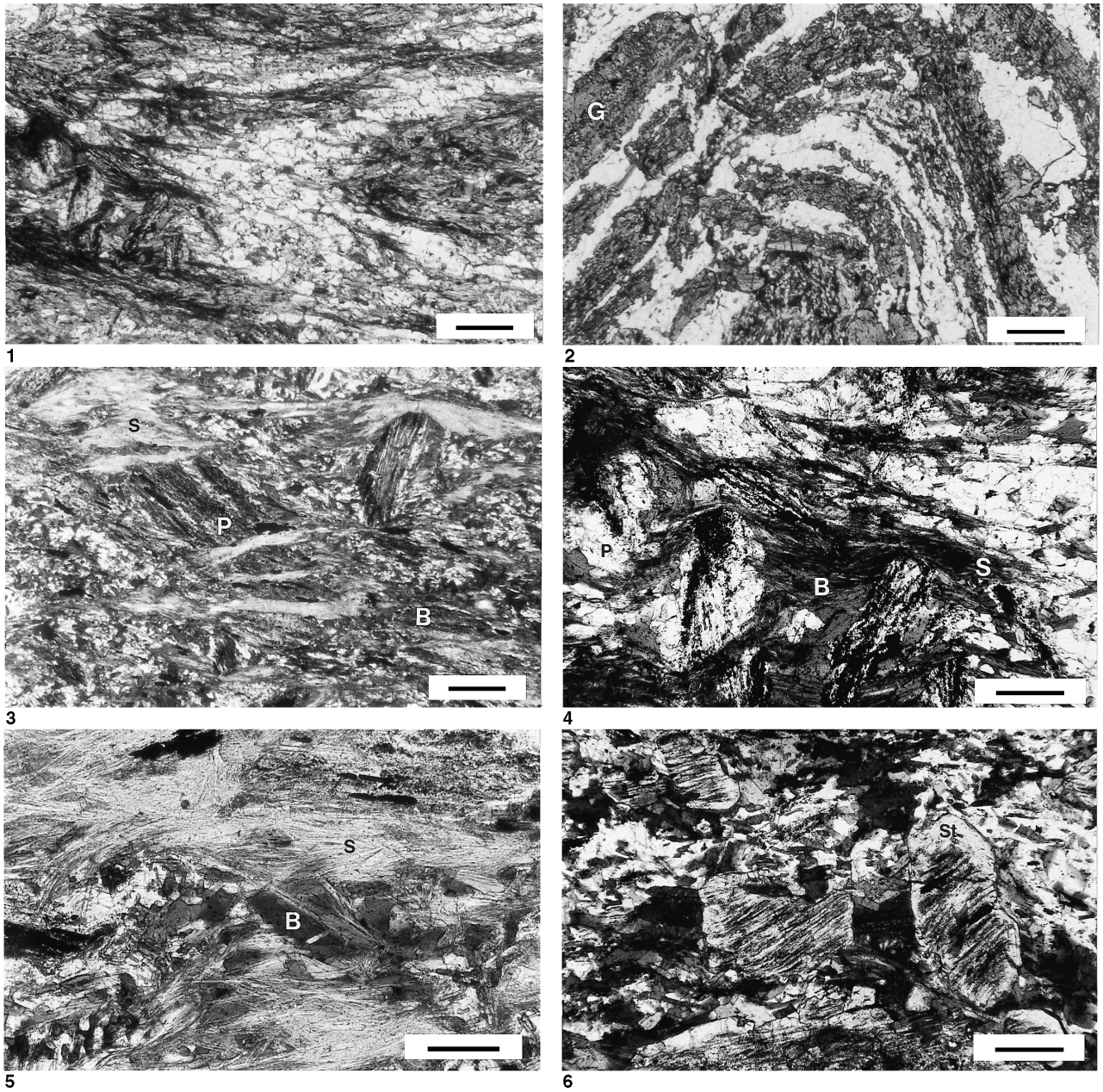

Plate 1. Selected key textural relationships in the high-grade schist. **1.** D_2 fold in a biotite-rich high-grade schist. Sillimanite and biotite define S_2 parallel to the axial surface of the fold. Note on the lower left corner the early plagioclase porphyroblasts with dark graphitic inclusions defining the previous foliation S_1. Sample 161-976E-23R-2, 118–123 cm. Plane-polarized light. Scale bar is 500 µm. **2.** Detail of a D_2 fold deforming S_1. S_1 is defined by garnet-rich and quartz-rich laminae. Garnet I porphyroblasts (G) have a typical skeletal and tabular shape. Sample 161-976E-14R-3, 0–4 cm. Plane-polarized light. Scale bar is 500 µm. **3.** Large plagioclase porphyroblasts (P) with straight graphitic inclusion trails, suggesting plagioclase growth between D_1 and D_2 (plagioclase I). Sheaves of fibrolitic sillimanite (S) and oriented biotite porphyroblasts (B) define the S_2 foliation. Sample 161-976B-77R-2, 40–44 cm. Plane-polarized light. Scale bar is 500 µm. **4.** Large plagioclase porphyroblasts (P) with two stages of growth. These grains have graphite-rich cores (plagioclase I) indicating that they grew statically over an early foliation (S_1), and were subsequently rotated during D_2. Plagioclase rims usually contain inclusions of biotite and sillimanite parallel to the external S_2 foliation, indicating a late, post-D_2 growth of plagioclase (plagioclase II). Oriented aggregates of fibrolitic sillimanite (S) and biotite (B) define the S_2 in press. foliation. Sample 161-976E-23R-2, 118–123 cm. Plane-polarized light. Scale bar is 200 µm. **5.** Biotite porphyroblasts (B) closely related to harmonious fibrolite (S) defining the S_2 foliation. Note the occurrence of some fibrolite crystals with disharmonious textures. Sample 161-976B-77R-2, 40–44 cm. Plane-polarized light. Scale bar is 200 µm. **6.** Nontransformed, elongated staurolite porphyroblasts (St) with straight inclusion trails (rutile, ilmenite, and graphite) defining S_1. These trails are oblique to the external S_2 fabric, defined by oriented biotite, plagioclase, and sillimanite. Sample 161-976B-76R-1, 45–49 cm. Plane-polarized light. Scale bar is 200 µm.

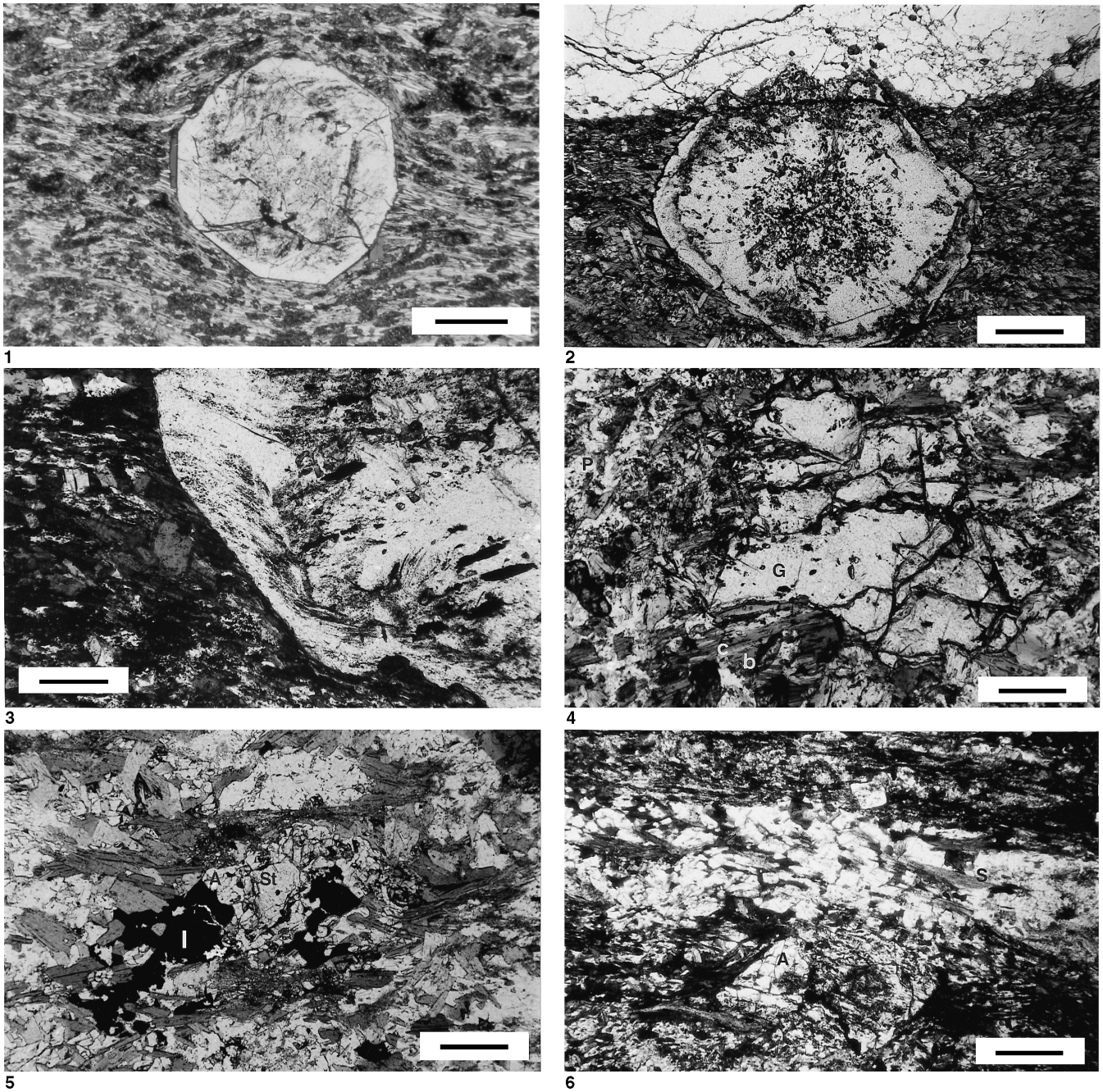

Plate 2. Selected key textural relationships in the high-grade schist. **1.** Garnet I porphyroblast surrounded by an idiomorphic rim of garnet II. Garnet I has graphitic and ilmenite inclusion trails defining a rotated internal foliation (S_1) oblique to the external foliation S_2. Garnet II rim is characterized by the lack of inclusions. Sample 161-976E-22R-1, 15–19 cm. Plane-polarized light. Scale bar is 500 µm. **2.** Example of irregular and sharp boundary between the garnet I (core) and garnet II (rim) zones, suggesting that resorption of garnet occurred between both growth stages. Sample 161-976E-15R-1, 2–7 cm. Plane-polarized light. Scale bar is 500 µm. **3.** Detail of garnet II rim with graphitic inclusions continuous with the external foliation S_2. Note the change of orientation of inclusion trails from rim (garnet II zone) to the outermost core (garnet I zone). Sample 161-976B-76R-1, 45–49 cm. Plane-polarized light. Scale bar is 200 µm. **4.** Garnet I porphyroblast (G) partially corroded by a fine-grained aggregate of chlorite (c), plagioclase (P), and quartz. Note how chlorite is also growing at expense of biotite (b). Sample 161-976E-14R-1, 98–102 cm. Plane-polarized light. Scale bar is 200 µm. **5.** Relic staurolite grain (St) partially included in andalusite (A), which also includes large ilmenite aggregates (I). Sample 161-976B-74X-1, 30–34 cm. Plane-polarized light. Scale bar is 200 µm. **6.** Andalusite porphyroblast (A) showing a postkinematic relationship to S_2, which is defined by oriented biotite and sillimanite (S) grains. Sample 161-976B-76R-2, 75–78 cm. Plane-polarized light. Scale bar is 500 µm.

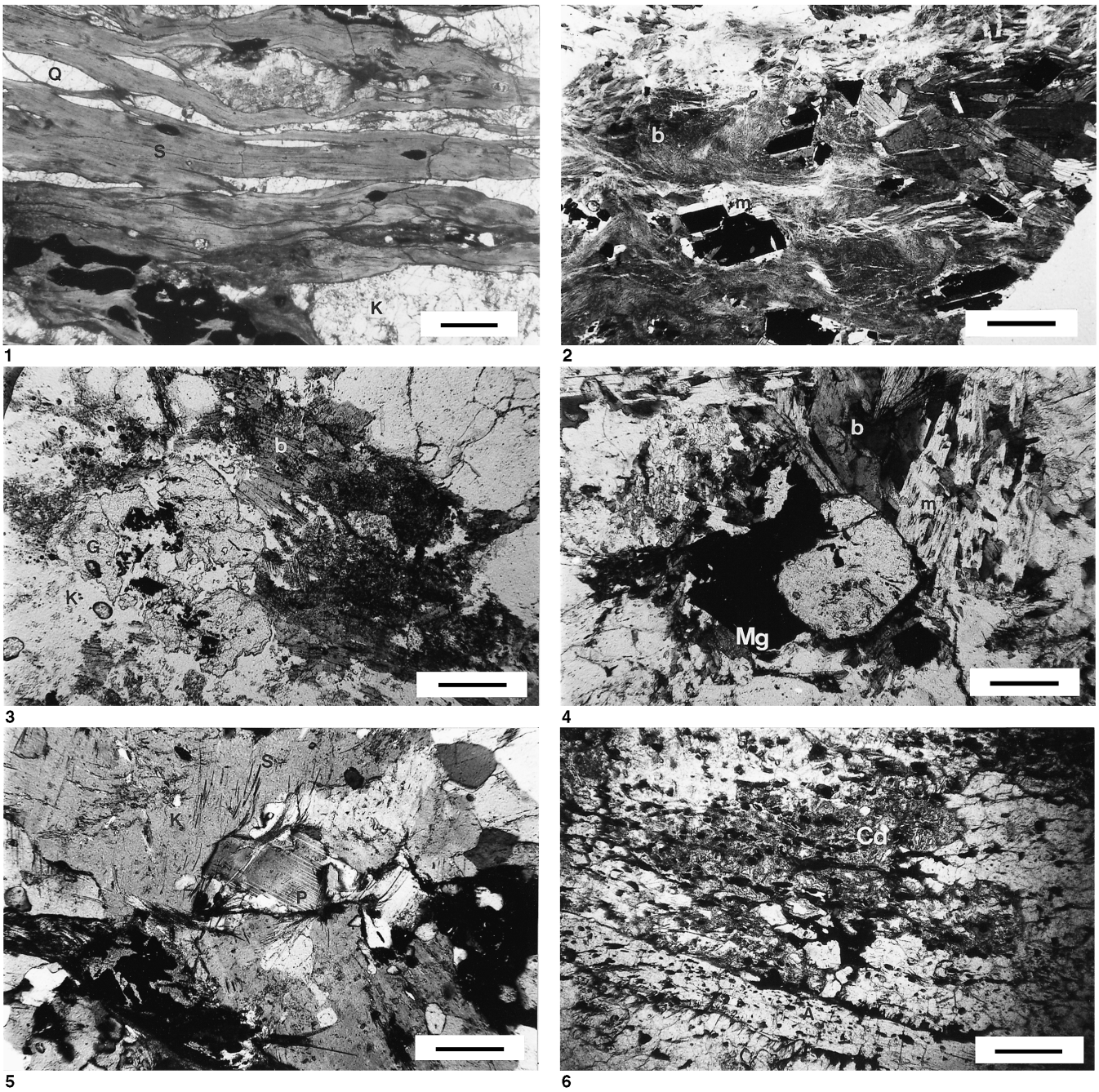

Plate 3. Selected key textural relationships in the pelitic and migmatite gneiss. **1.** Foliation defined by intensely oriented harmonious fibrolite (S) with augen of magnetite (black) and aggregates of quartz (Q) and K-feldspar (K). Sample 161-976B-95R-2, 24–28 cm. Plane-polarized light. Scale bar is 500 µm. **2.** Idiomorphic magnetite crystals (black) surrounded by muscovite (m) and decussate aggregates of biotite (b). Sample 161-976B-98R-1, 38–40 cm. Plane-polarized light. Scale bar is 200 µm. **3.** Relic garnet porphyroblast (garnet I) largely corroded by biotite (b) and K-feldspar (K). Sample 161-976B-98R-1, 38–40 cm. Plane-polarized light. Scale bar is 200 µm. **4.** Subidiomorphic garnet porphyroblast (garnet II) surrounded by magnetite (Mg) and biotite (b), which is partially transformed to muscovite (m). Sample 161-976B-98R-1, 96–101 cm. Plane-polarized light. Scale bar is 200 µm. **5.** Example of disharmonious fibrolite (S) included in large K-feldspar (K) and plagioclase (P) phenocrysts. Leucosome domain of a migmatitic gneiss. Sample 161-976B-95R-2, 24–28 cm. Cross-polarized light. Scale bar is 200 µm. **6.** Late irregular spongy porphyroblast of cordierite (Cd) including quartz, fibrolite, and ilmenite, which define the main foliation in the rock. Cordierite is largely transformed to pinnite. Large idiomorphic andalusite porphyroblast (A) is oriented parallel to the main foliation. Sample 161-976B-101R-1, 86–89 cm. Plane-polarized light. Scale bar is 500 µm.

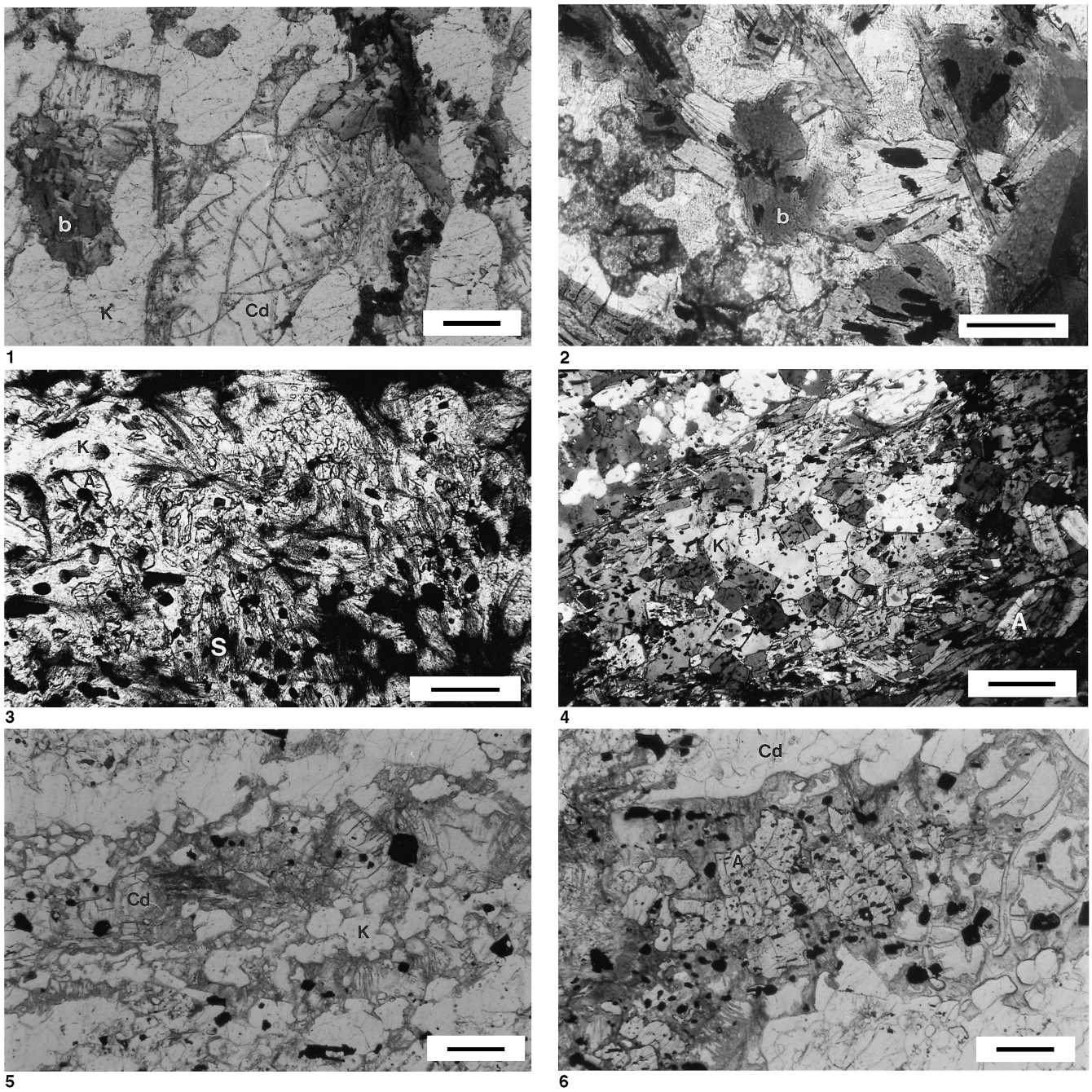

Plate 4. Selected key textural relationships in the pelitic and migmatite gneiss. **1.** Leucosome domain of a migmatite gneiss formed by cordierite (Cd) interfingered with K-feldspar (K), plagioclase, biotite (b), and quartz. Sample 161-976B-98R-1, 96–101 cm. Plane-polarized light. Scale bar is 500 µm. **2.** Decussate clusters of biotite (b) in leucosome domain, with abundant inclusions of elongated magnetite and Ti-magnetite grains. Sample 161-976B-98R-1, 96–101 cm. Plane-polarized light. Scale bar is 200 µm. **3.** Rounded andalusite porphyroblasts (A) included with disharmonious fibrolitic sillimanite (S) in a large K-feldspar phenocryst (K). Sample 161-976B-101R-2, 38–41 cm. Plane-polarized light. Scale bar is 200 µm. **4.** Idiomorphic and zoned andalusite phenocrysts included in a large K-feldspar grain (K). Sample 161-976B-96R-1, 46–48 cm. Cross-polarized light. Scale bar is 500 µm. **5.** Mutual intergrowths between cordierite (Cd) and the granitic matrix, composed by K-feldspar (K), quartz, and minor plagioclase phenocrysts. Sample 161-976B-96R-1, 46–48 cm. Plane-polarized light. Scale bar is 500 µm. **6.** Andalusite porphyroblasts (A) included in a large cordierite grain (Cd), partially retrograded to pinnite. Sample 161-976B-96R-1, 46–48 cm. Plane-polarized light. Scale bar is 500 µm.